

# Optical follow-up observation of Fast Radio Burst 151230

Nozomu TOMINAGA<sup>1,2</sup>, Yuu NIINO<sup>3</sup>, Tomonori TOTANI<sup>4,5</sup>, Naoki YASUDA<sup>2</sup>, Hisanori FURUSAWA<sup>3</sup>, Masayuki TANAKA<sup>3</sup>, Shivani BHANDARI<sup>6,7,8</sup>, Richard DODSON<sup>9</sup>, Evan KEANE<sup>10</sup>, Tomoki MOROKUMA<sup>11</sup>, Emily PETROFF<sup>12</sup> and Andrea POSSENTI<sup>13</sup>

<sup>1</sup>Department of Physics, Faculty of Science and Engineering, Konan University, 8-9-1 Okamoto, Kobe, Hyogo 658-8501, Japan

<sup>2</sup>Kavli Institute for the Physics and Mathematics of the Universe (WPI), The University of Tokyo Institutes for Advanced Study, The University of Tokyo, 5-1-5 Kashiwa, Chiba 277-8583, Japan

<sup>3</sup>National Astronomical Observatory of Japan, 2-21-1 Osawa, Mitaka, Tokyo 181-8588, Japan

<sup>4</sup>Department of Astronomy, School of Science, The University of Tokyo, 7-3-1 Hongo, Bunkyo-ku, Tokyo 113-0033, Japan

<sup>5</sup>Research Center for the Early Universe, School of Science, The University of Tokyo, 7-3-1 Hongo, Bunkyo-ku, Tokyo 113-0033, Japan

<sup>6</sup>CSIRO Astronomy and Space Science, PO Box 76, Epping, NSW 1710, Australia

<sup>7</sup>Centre for Astrophysics and Supercomputing, Swinburne University of Technology, Mail H30, PO Box 218, VIC 3122, Australia

<sup>8</sup>ARC Centre of Excellence for All-sky Astrophysics (CAASTRO), Australia

<sup>9</sup>International Centre for Radio Astronomy Research, The University of Western Australia, 35 Stirling Hwy, Western Australia

<sup>10</sup>SKA Organisation, Jodrell Bank Observatory, Macclesfield, Cheshire, SK11 9DL, UK

<sup>11</sup>Institute of Astronomy, Graduate School of Science, The University of Tokyo, 2-21-1 Osawa, Mitaka, Tokyo 181-0015, Japan

<sup>12</sup>ASTRON Netherlands Institute for Radio Astronomy, Oude Hoogeveensedijk 4, 7991PD Dwingeloo, The Netherlands

<sup>13</sup>INAF-Osservatorio Astronomico di Cagliari, Via della Scienza 5, I-09047 Selargius (CA), Italy

\*E-mail: tominaga@konan-u.ac.jp

Received 2018 April 19; Accepted 2018 August 9

## Abstract

The origin of fast radio bursts (FRBs), bright millisecond radio transients, is still somewhat of a mystery. Several theoretical models expect that the FRB accompanies an optical afterglow (e.g., Totani 2013; Kashiyama et al. 2013). In order to investigate the origin of FRBs, we perform *gri*-band follow-up observations of FRB 151230 (estimated  $z \lesssim 0.8$ ) with Subaru/Hyper Suprime-Cam at 8, 11, and 14 days after discovery. The follow-up observation reaches a 50% completeness magnitude of 26.5 mag for point sources, which is the deepest optical follow-up of FRBs to date. We find 13 counterpart candidates with variabilities during the observation. We investigate their properties with multicolor and multi-wavelength observations and archival catalogs. Two candidates are excluded by the non-detection of FRB 151230 in the other radio

feed horns that operated simultaneously to the detection, as well as the inconsistency between the photometric redshift and that derived from the dispersion measure of FRB 151230. Eight further candidates are consistent with optical variability seen in AGNs. Two more candidates are well fitted with transient templates (Type II<sub>n</sub> supernovae), and the final candidate is poorly fitted with all of our transient templates and is located off-center of an extended source. It can only be reproduced with rapid transients with a faint peak and rapid decline and the probability of chance coincidence is  $\sim 3.6\%$ . We also find that none of our candidates are consistent with Type Ia supernovae, which rules out the association of Type Ia supernovae to FRB 151230 at  $z \leq 0.6$  and limits the dispersion measure of the host galaxy to  $\lesssim 300 \text{ pc cm}^{-3}$  in a Type Ia supernova scenario.

**Key words:** Radio continuum: general — Methods: observational — Surveys — supernovae: general — Pulsars: general — Stars: general

## 1 Introduction

Fast radio bursts (FRBs) are bright millisecond radio transients that were first discovered in a search of archival data of the Parkes Radio Telescope (Lorimer et al. 2007). Subsequent searches discovered further FRBs with the Parkes Radio Telescope (e.g., Champion et al. 2016), the Green Bank Telescope (Masui et al. 2015), the Arecibo Telescope (Spitler et al. 2014), the Molonglo Observatory Synthesis Telescope (Caleb et al. 2017), and the Australian SKA Pathfinder (Bannister et al. 2017); information on all FRBs is listed in the FRB Catalogue (Petroff et al. 2016).<sup>1</sup> The defining characteristic of FRBs is a dispersion measure (DM) in excess of what can be explained by the Milky Way. If this excess is attributed to free electrons in the intergalactic medium (IGM), FRBs could thus conceivably be used to probe the so-called “missing” baryon and magnetic fields and turbulence in the IGM (e.g., Ravi et al. 2016). The observed rate of FRBs is at least as high as  $5 \times 10^3 \text{ sky}^{-1} \text{ day}^{-1}$  (Bhandari et al. 2018).

However, the origin of FRBs is still unknown. There are many theoretical proposals; for example, mergers of double neutron star binaries (Totani 2013), mergers of double white dwarf binaries (Kashiyama et al. 2013)<sup>2</sup>, the collapse of rotating supermassive neutron stars to black holes (Falcke & Rezzolla 2014; Zhang 2014), exotic Galactic compact objects (Keane et al. 2012; Bannister & Madsen 2014), interactions between the supernova shock and magnetosphere of a neutron star (Egorov & Postnov 2009), compact objects in young supernovae (Connor et al. 2016; Piro 2016), supergiant pulses from extragalactic neutron stars (Cordes & Wasserman 2016), and giant flares from magnetars (Thornton et al. 2013; Pen & Connor 2015).

Observationally, most FRBs are non-recurrent, with the exception of FRB 121102 (Spitler et al. 2014; Spitler et al. 2016).

Thanks to its repeatability, radio interferometric observations of its bursts have achieved a subarcsecond localization and identify a faint and persistent optical counterpart (Chatterjee et al. 2017). Follow-up observations reveal that the host galaxy is an irregular and low-metallicity dwarf galaxy at  $z = 0.19$  and does not show optical signatures of AGN activity (Marcote et al. 2017; Tendulkar et al. 2017) and that the source of FRB 121102 is spatially coincident with a star-forming region (Bassa et al. 2017; Kokubo et al. 2017). These observations are consistent with the proposal of newly born neutron stars as the origin of FRBs. Unlike FRB 121102 no repeat emission has yet been discovered in the other FRBs despite considerable effort (Lorimer et al. 2007; Ravi et al. 2015; Petroff et al. 2015a).

Owing to the large single-dish telescopes used to discover FRBs, localization is typically  $\sim 15$  arcmin, and there are a large number ( $> 10^4$ ) of galaxies in the localized region. In order to clarify the origin of FRBs, the first step is a precise localization with telescopes which have better spatial resolution. In scenarios involving coincident optical emission this can be achieved by using wide-field optical telescopes to monitor FRB fields. The SURvey for Pulsars and Extragalactic Radio Bursts (SUPERB) operates a realtime data analysis pipeline issuing realtime alerts (Keane et al. 2018; Bhandari et al. 2018). This enables searches for contemporaneous variability in the radio, or other wavelengths, or indeed in other windows of observation such as neutrinos or gravitational waves. Previously Keane et al. (2016) reported a variable radio source in the field of FRB 150418, which was thought to be a fading counterpart associated with the FRB, but continued longer-term monitoring revealed a persistent radio source with short timescale variability (Williams & Berger 2016; Johnston et al. 2017). The variability and the location are consistent with an active galactic nuclei at the galaxy’s center (Akiyama & Johnson 2016; Bassa et al. 2016) but it is unclear if this is truly associated with the FRB event, or more generally how FRBs and AGN could be associated (see e.g., Vieyro et al. 2017).

<sup>1</sup> <http://frbcat.org/>

<sup>2</sup> They assume that the emitting region is a portion of the merged white dwarf to reproduce the short duration of FRBs.

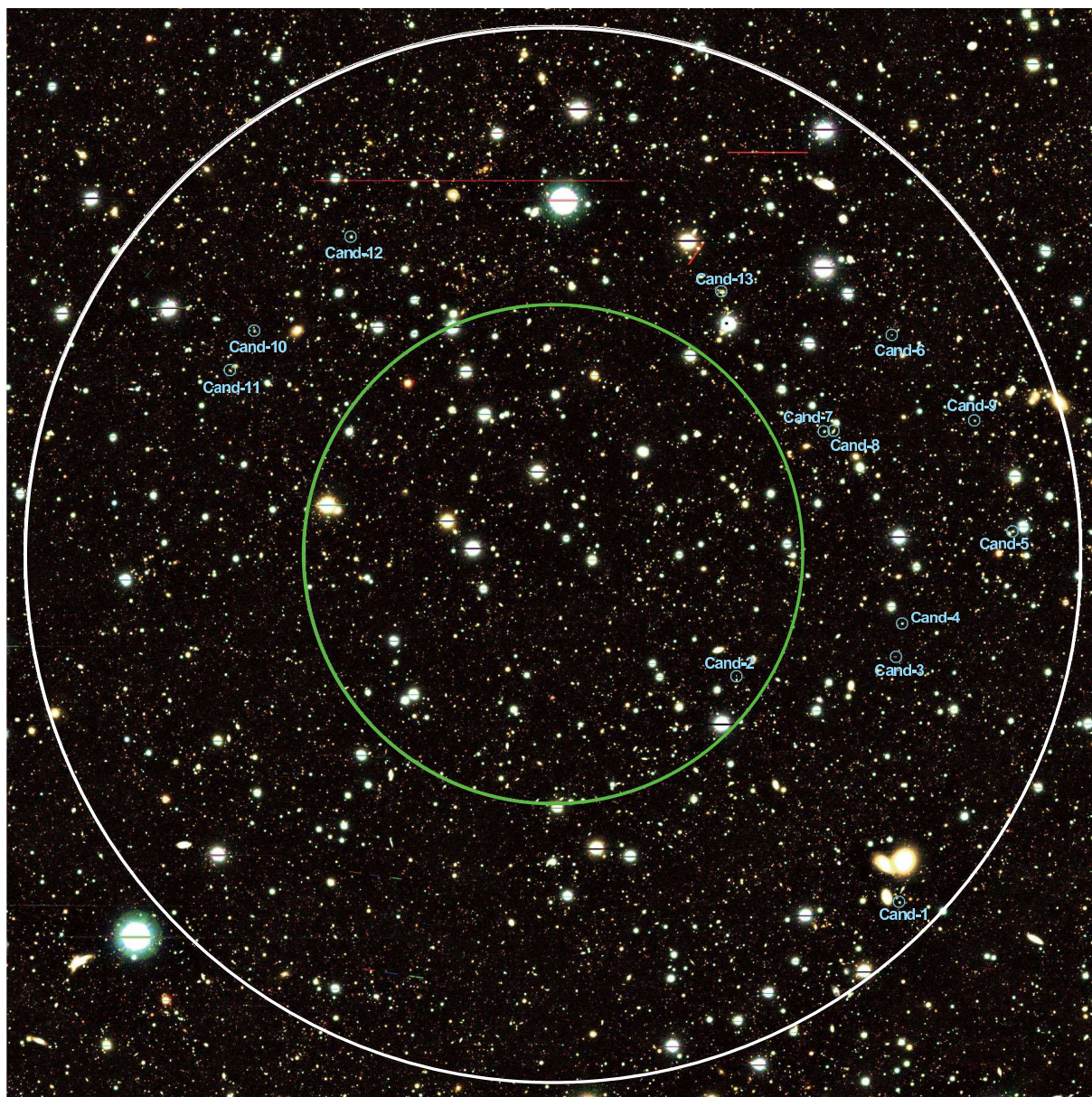


**Fig. 1.** Three color image on Day 14 of a part of a field followed-up with HSC centered at the central position of the beam 04. The FWHM of beam profile and the localization area adopted in this paper are shown in a green circle with a radius of 7.05 arcmin and a white circle with a radius of 15 arcmin, respectively. The locations of 13 final candidates are shown in cyan circles.

After a realtime alert from the SUPERB collaboration, we performed optical imaging observations of FRB 151230 detected in beam 04 of the Parkes multi-beam receiver (Manchester et al. 2001). This FRB has a DM of  $960.4 \pm 0.5 \text{ pc cm}^{-3}$  corresponding to an estimated redshift of  $\sim 0.8$  assuming it lies along an average line of sight through the Universe (Bhandari et al. 2018). An optical afterglow is expected by some theoretical models, e.g., the merger of double neutron star binaries and double white dwarf binaries. We use Subaru/Hyper Suprime-Cam (HSC, Miyazaki et al. 2012; Miyazaki et al. 2018) that is a unique wide-field camera on an 8m-class telescope with a field of view of  $1.77 \text{ deg}^2$  and a pixel size of 0.17 arcsec. The HSC has the highest survey power per unit time of any optical telescope and its field of view is 40 times larger than the typical localization of FRBs. Thus it is the most powerful instrument for the follow-up observations of FRB fields in the optical.

This paper consists of the following sections. In Section 2, the observations and data analyses are described. In Section 3, we present multicolor light curves of candidates possibly associated with FRB 151230, and discuss their nature. In Section 4, we describe constraints on the association between FRB 151230 and Type Ia supernova (SN Ia) from the observations. In Section 5, a discussion and our conclusions are presented. In this paper, we adopt the AB magnitude system unless otherwise noted and the fiducial cosmology with  $H_0 = 70 \text{ km s}^{-1} \text{ Mpc}^{-1}$ ,  $\Omega_\lambda = 0.7$ , and  $\Omega_M = 0.3$ .

## 2 Observations and data reduction

FRB 151230 was discovered at 2015-12-30 16:15:46 (UT) at 1.4 GHz at R.A. =  $09^{\text{h}}40^{\text{m}}50^{\text{s}}$ , decl. =  $-03^{\circ}27'05''$  (J2000.0) with an uncertainty of  $\sim 15$  arcmin diameter which corresponds to the full width at half maximum (FWHM) of the receiver beam pattern (Figure 1). In this paper, in order to not miss candidates outside the FWHM radius, we take a radius of 15 arcmin to judge whether a candidate is located in the localization area of FRB 151230. The FRB's true position is very unlikely to be beyond this radius unless the source count slope is unrealistically steep (Macquart & Ekers 2018). Hereafter, we call this circle the localization area of FRB 151230. The mean Galactic color excess within a circle of 5 arcmin radius in this direction is  $E_{B-V, \text{Gal}} = 0.039 \text{ mag}$  (Schlafly & Finkbeiner 2011),<sup>3</sup> although there is a small scatter in this value of  $\sim 0.005 \text{ mag}$  across the localization. The extinction in the host galaxies is not corrected. We performed HSC  $g$ -,  $r$ -, and  $i$ -band follow-up imaging observations with 50 – 70 min exposures on Jan 7, 10, and 13, 2016 (UT, Days 8, 11, and 14 after FRB 151230). Each exposure consists of multiple 3.5- or 4-min shots with dithering. The FWHMs of the point spread function (PSF) range from

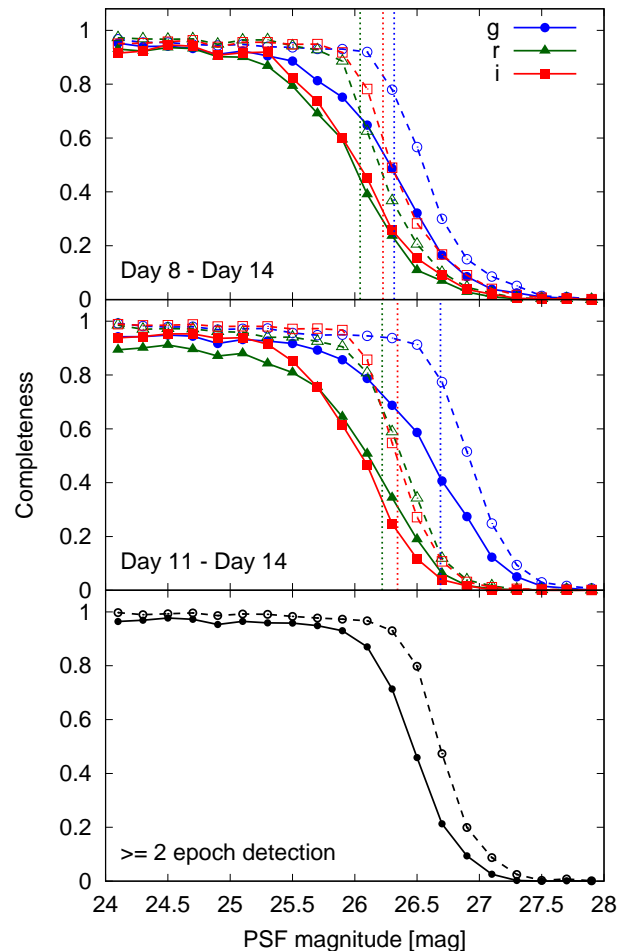


Fig. 2. Completeness of source detection in the difference images on Day 8 – 14 (top) and Day 11 – 14 (middle), and in the 6 difference images (bottom). The dashed and solid lines represent completeness before and after the source screening, respectively. The vertical dotted lines show the  $5\sigma$  limiting magnitude in the difference images.

0.7 to 1.4 arcsec. The observation details are summarized in Table 1.

The data is reduced using HSC pipeline version 4.0.5 (Bosch et al. 2017), which is based on the LSST pipeline (Ivezic et al. 2008; Axelrod et al. 2010; Jurić et al. 2015). It provides packages for bias subtraction, flat fielding, astrometry, flux calibration, mosaicing, warping, stacking, image subtraction, source detection, and source measurement. The astrometric and photometric calibration is made relative to the Pan-STARRS1 (PS1, Chambers et al. 2016) with a 4.0 arcsec (24-pixel) aperture diameter. The images after CCD processing are warped to the predefined skymap with a pixel size of 0.17 arcsec and the calibrated images are then stacked with a direct weighted average.

We estimate the  $5\sigma$  limiting magnitudes of the  $gri$  stacked images in the localization area of FRB 151230 on Days 8, 11, and 14 using between 90 and 600 apertures with a diameter of twice the FWHM size of PSF (Table 1). Here, we distribute randomly and independently the apertures on the sky area with-

<sup>3</sup> <http://irsa.ipac.caltech.edu/applications/DUST/>

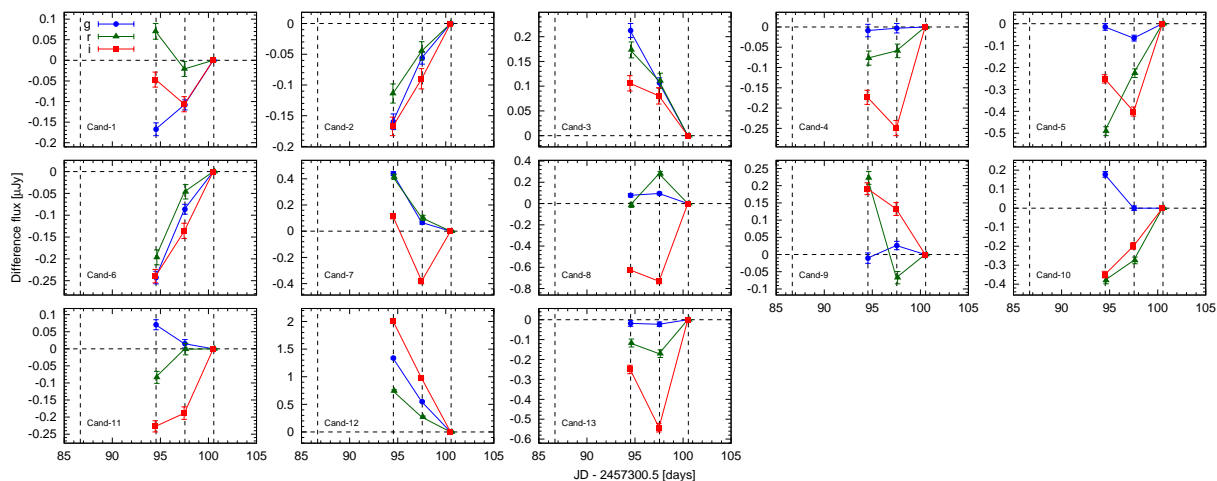


Fig. 3. Difference light curves of the 13 final candidates. The vertical lines represents the event time of FRB 151230 and the epochs of the HSC observations.

out any detection of sources and subtract the local sky flux from the aperture flux. The  $5\sigma$  limiting magnitudes in the localization area of FRB 151230 range from 26.0 mag to 27.3 mag (Table 1). The deepest observation on Day 10 detects  $\sim 190,000$  sources in the localization area of FRB 151230.

In order to select variable objects, we perform image subtraction between the stacked images. The images taken on Day 14 are set as the reference images and are subtracted from the science images taken on Days 8 and 11 because a time-variable object would typically have a larger differential flux over a longer time interval. The images with narrower PSF between reference and science images are convolved with kernels to make their PSFs equivalent (Alard & Lupton 1998). The  $5\sigma$  limiting magnitudes of the difference images in the localization area of FRB 151230 are estimated with randomly and independently distributed apertures with a diameter of twice the FWHM size of the PSF. As the image subtraction between images with similar depths result in a shallower depth than the original images, the  $5\sigma$  limiting magnitudes of the difference images range from 25.8 mag to 26.3 mag. We also evaluate detection completeness by random injection and detection of artificial point sources with various magnitudes (Figure 2). The  $5\sigma$  limiting magnitudes are comparable to the PSF magnitude at 50 – 70% completeness. The  $5\sigma$  limiting magnitudes and the 50% completeness magnitudes in the difference images are summarized in Table 2.

Point sources in the difference images are detected and measured with the HSC pipeline. Since there are many false positives due to noise, we adopt the following criteria to identify bona fide sources; (1) significance higher than  $5\sigma$ , (2)  $(b/a)/(b/a)_{\text{PSF}} > 0.65$  where  $a$  and  $b$  are the lengths of the major and minor axes of a shape of a source, respectively, (3) FWHM of a source is between 0.7 to 1.3 times that of the PSF, (4) the residual of PSF subtraction from a source is  $< 3\sigma$ . These criteria are similar to those adopted in searches for op-

tical counterparts of gravitational wave signals (Utsumi et al. 2018; Tominaga et al. 2018). After this screening, 118 and 1078 variable sources remain inside and outside the localization area of FRB 151230, respectively. We also estimate the detection completeness after the screening with injected artificial sources. The 50% completeness magnitudes after the screening are 0.2-0.4 mag shallower than those before owing to low signal-to-noise ratios (S/N). We further imposed the sources be detected at least twice at the same location in the 6 difference images. The 50% completeness magnitude after this additional screening is 26.5 mag for point sources, which is the deepest among all the optical follow-up observations of FRBs which cover the entire localization area (Petroff et al. 2015b; Keane et al. 2016; Bhandari et al. 2018).

The PSF shape in the stacked images sometimes fails the image subtraction at the center of galaxies leaving an unphysical residual. Thus, we also perform an alternative procedure of image subtraction; the stacked reference image is subtracted from each exposure of the science images and the resultant difference images are stacked. If the source is located within a separation of 0.34 arcsec (2 pixel) from objects in the stacked images or objects in the PS1 catalog, we check whether the source is detected in the alternative procedure. Here, the positions of objects in the stacked images are measured with the HSC pipeline at the epoch when the source is faintest. We exclude the source if it is not detected in the alternative procedure. After this exclusion, 53 variable sources inside the localization area of FRB 151230 and 490 variable sources outside the localization area of FRB 151230 remain, respectively. However, false positives, e.g., failures of image subtraction around bright objects (e.g., Figure 1 in Morii et al. 2016), still remain. Therefore, we visually inspect the variable sources to remove these, and select 13 sources inside the localization area of FRB 151230 as the final candidates. These are summarized in Table 3. Transients outside the localization area of FRB 151230 are described in

Appendix 1.

Difference light curves of candidates are derived with forced PSF photometry of the difference images with aperture correction at the location of candidates and dereddening for the Galactic extinction. Figure 3 shows their difference light curves. We also measure the PSF fluxes at the location of candidates in the stacked images with forced PSF photometry. The forced PSF flux in the stacked image is an upper limit of the flux of the candidate because it consists of the fluxes of both the candidate and its host galaxy.

### 3 Nature of candidates

After the source screening and the visual inspection, 13 final candidates remain. Their locations are shown in Figure 1.

#### 3.1 Light curve fitting and locations within galaxies

In order to investigate the nature of the candidates with the limited available data over  $\sim 1$  week, we primarily perform the difference light curve fitting described in Appendix 2. For this, we adopt templates of SNe Ia (Hsiao et al. 2007), core-collapse SNe (CCSNe; Type Ibc, IIP, IIL, and IIn SNe, Nugent et al. 2002), and rapid transients (RTs, from the gold sample in Drout et al. 2014).<sup>4</sup> We take into account a variation of the explosion date  $t_{\text{exp}}$  of templates since the occurrence time of FRB 151230 and an intrinsic variation of templates, e.g., peak absolute magnitude and extinction in the host galaxy. In order to judge the agreement of the template fitting, we employ  $Q(\chi^2|\nu)$  value, the probability that a  $\chi^2$  distribution with a degree of freedom  $\nu$  exceeds a given  $\chi^2$  value by chance.

In addition to the difference light curve fitting, if the flux of the host galaxy is likely to dominate the flux of the candidate, we adopt the photometric redshift of the host galaxy as a criterion to narrow down the possible templates and impose that the redshift derived from the difference light curve fitting be consistent with the photometric redshift. The photometric redshift is derived with the *gri* photometry of the host galaxy in the stacked images using a photometric redshift code with Bayesian priors on physical properties of galaxies (Tanaka 2015). Further, a separation of each candidate from its host galaxy (if existing) is employed to exclude the possibility of active galactic nuclei (AGN) and Galactic stars. We conservatively adopt both the position measured with the HSC pipeline and the position of a pixel with a peak count in a  $10 \text{ pix} \times 10 \text{ pix}$  square centered on the candidate as the possible position of the associated object in the stacked images at the epoch when each candidate is faintest.

In this subsection, we focus on candidates that can be distin-

guished from optical variability typical of AGNs. As any optical counterpart to FRB 151230 need not have a light curve of known form, we consider (1) candidates reproduced with transient templates with a loose criterion  $Q > 10^{-4}$  because our aim is only to narrow down possible templates, or (2) candidates located off-center of their host galaxy with a separation of  $> 0.34$  arcsec. After applying the above steps, we pick up 4 candidates (Table 4). Nine of the 13 candidates are consistent with optical variability from AGN, and we discard them from further investigation and focus on these 4 candidates in this subsection. Of the remaining 4, 3 candidates are well fitted by the transient templates with  $Q > 10^{-4}$ .

#### 3.1.1 Candidates consistent with transient templates

Three candidates, Cand-2, Cand-6, and Cand-11, are well fitted with the transient templates. These candidates are associated with extended objects, presumably galaxies (Figure 4). Their separations from the center of the localization area of FRB 151230 are 6.24 arcmin for Cand-2, 11.43 arcmin for Cand-6, and 10.55 arcmin for Cand-11. As the fluxes in the stacked images are dominated by the fluxes of their host galaxies (Table 1), we derive the photometric redshifts of the host galaxies adopting the fluxes on Day 8, on which the contributions of the 3 candidates to the total fluxes are relatively small. The photometric redshifts of the host galaxies of Cand-2, Cand-6, and Cand-11 are  $z = 0.18_{-0.15}^{+0.46}$ ,  $1.44_{-0.27}^{+0.46}$ , and  $0.19_{-0.15}^{+0.07}$ , respectively. Here, we adopt the 95% probability as the errors. The photometric redshift of the host galaxy of Cand-6 is inconsistent with the maximum redshift inferred from the DM of FRB 151230 and thus Cand-6 is unlikely to be an optical counterpart of FRB 151230. However, in the next paragraph, we also describe the templates consistent with Cand-6 for comparisons with a theoretical estimate and the total number of candidates outside the localization area.

The best-fit templates within the 95% probability of the photometric redshift are an RT (PS1-10ah) at  $z = 0.60$  for Cand-2, an SN IIn at  $z = 1.25$  for Cand-6, and an SN IIn at  $z = 0.10$  for Cand-11 (Figure 5). We also derive probable templates and possible ranges of parameters allowing the template with the  $Q$  value of  $> 0.01$  of the maximum  $Q$  value for each candidate. While Cand-6 and Cand-11 can be fitted only with the SN IIn template, Cand-2 can also be fitted with SN IIP and IIn templates in addition to the best-fit RT template (Table 4). As the difference of the  $Q$  values of Cand-2 between the RT and SN IIn templates is only a factor of 2, an SN IIn is a comparably good fit to an RT for the origin of Cand-2. The location of the candidate can be used to constrain the possibility of an AGN origin. While Cand-2 is located off-center of the galaxy, Cand-11 is located at the center of the host galaxy and thus optical variability of an AGN cannot be excluded. The most probable templates for Cand-2 include those with  $t_{\text{exp}} \sim 0$  day. If Cand-2 exploded

<sup>4</sup> We exclude PS1-12bb from the sample because it does not have the data points before the peak.

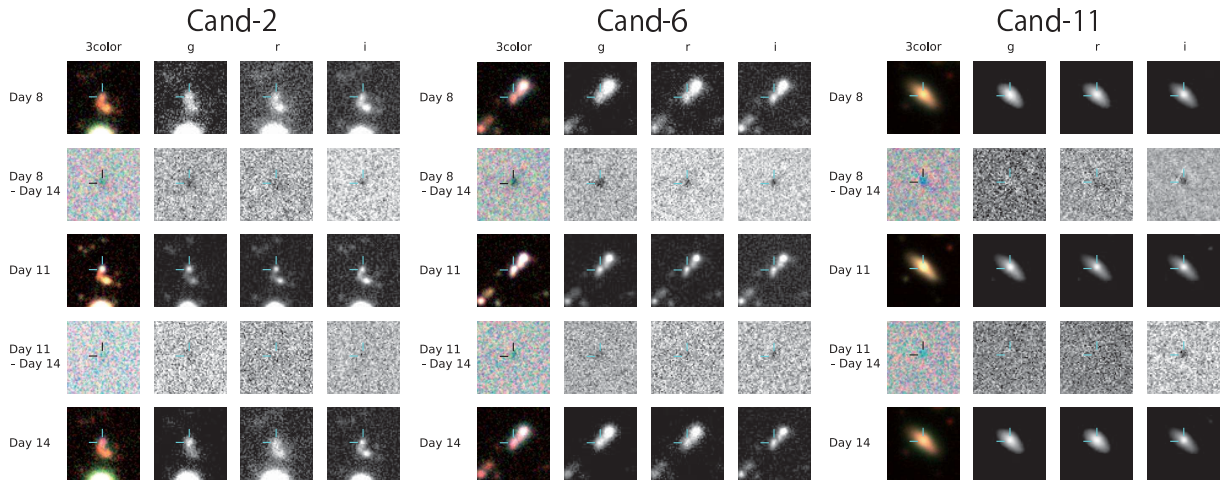


Fig. 4. Images at the location of the candidates fitted with the transient templates (ticks). The lengths of ticks are 1 arcsec and the figure size is  $10 \times 10$  arcsec<sup>2</sup>.

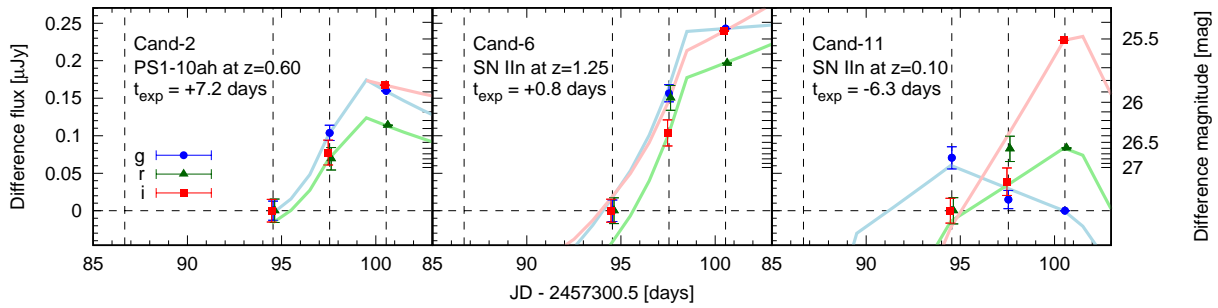


Fig. 5. Comparisons of the difference light curves of the candidates and the best-fit templates. The fluxes are shifted to be zero at the faintest epoch.

at the same date as FRB 151230, the achromatic and rapid rising of Cand-2 is only consistent with SNe IIn, while the RT templates agree with the multicolor light curves of Cand-2 only for  $t_{\text{exp}} = +7.2_{-0.5}^{+1.1}$  days.

### 3.1.2 A candidate inconsistent with transient templates

The multicolor light curves of an off-center candidate, Cand-3, cannot be reproduced with any of our transient templates. Cand-3 is located 0.43 arcsec away from the center of its host galaxy, and 10.15 arcmin from the center of the localization area of FRB 151230 (Figure 6). Its off-center nature indicates that Cand-3 is likely not due to optical variability of an AGN. As the contribution of Cand-3 to the total flux in the stacked image is not negligible, we can not evaluate the photometric redshift of the host galaxy.

The best-fit template is an RT template (PS1-11qr) being +0.9 mag fainter than PS1-11qr and having  $Q = 2.2 \times 10^{-6}$  (Table 4). The low  $Q$  value stems mainly from the poor agreement in the  $i$ -band difference light curve (Figure 7a). The most probable template other than PS1-11qr is also an RT template (PS1-12brf) being +0.45 mag fainter than PS1-12brf with  $Q = 2.3 \times 10^{-8}$ . On the other hand, comparisons with SN Ia and CCSN templates result in a  $Q$  value of  $< 10^{-21}$ .

The forced PSF magnitudes of Cand-3 in the stacked images

indicate a  $g$ -band decline rate of  $> +0.23$  mag day<sup>-1</sup> in the observer frame. The rate is consistent with the rest-frame decline of the most rapidly-declining RTs in Drout et al. (2014). Although this could be consistent with kilonova emission from binary neutron stars coalescence (Utsumi et al. 2017), the blue color of Cand-3 on Day 8 is inconsistent with that regardless of the occurrence date because a kilonova with lanthanoid production is red in optical 0.5 days after the coalescence and becomes redder with time (e.g., Pian et al. 2017). These results demonstrate that the multicolor light curves of Cand-3 can be reproduced only by the RT templates. We also note that, if we set the criterion to be  $Q > 2 \times 10^{-6}$ , there are no candidates fitted with the RT templates other than Cand-2 and Cand-3, and Cand-4 is fitted with an SN IIL template with  $Q = 5.8 \times 10^{-5}$ .

The reason why Cand-3 is not reproduced with the transient templates is the small fluxes in the stacked images, which are faint especially on Day 11 and 14. This could be resolved if Cand-3 has fainter peak magnitude and/or more rapid decline than the RTs observed so far. Since the distribution of the peak magnitude and decline rate of RTs is still not well-known, we test the difference light curve fitting stretching a timescale parameter of the RT templates. Here, we reduce the stretch factor  $s$  from 1.0 to 0.05 in steps of 0.05. Doing this, agreement be-

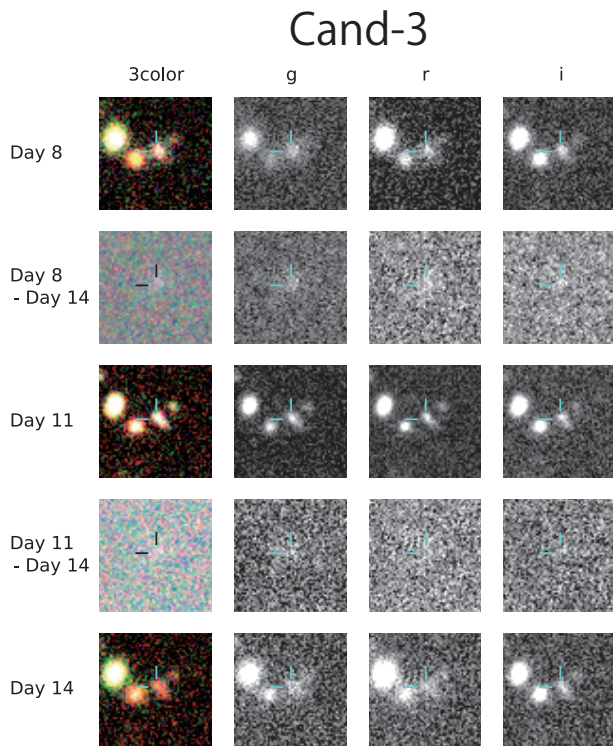


**Fig. 6.** Images at the location of Cand-3 (ticks) that is located at the off-center of extended objects. The lengths of ticks are 1 arcsec and the figure size is  $10 \times 10$  arcsec<sup>2</sup>.

tween Cand-3 and RT templates with  $Q > 10^{-4}$  can be realized in the range  $0.15 \leq s \leq 0.8$  with the best agreement achieved with  $s = 0.6$ . The best-fit templates with  $s = 0.8$  and  $0.6$  are shown in Figures 7(b) and 7(d), and the probable templates with  $s = 0.8$  and  $0.6$  are summarized in Table 5. For  $s = 0.8$ , the best-fit template is the PS1-10ah template at  $z = 0.2$ , which is  $+1.0$  mag fainter than PS1-10ah, and has  $Q = 7.4 \times 10^{-4}$ . The possible ranges of  $t_{\text{exp}}$  and  $z$  are  $t_{\text{exp}} = -1.4_{-2.5}^{+7.5}$  days and  $z = 0.20_{-0.03}^{+0.68}$ , respectively. For  $s = 0.6$ , the best-fit template is the PS1-10bjp template at  $z = 0.4$ ,  $+1.0$  mag fainter than PS1-10bjp, and with  $Q = 4.2 \times 10^{-1}$ . The possible ranges of  $t_{\text{exp}}$  and  $z$  are  $t_{\text{exp}} = +5.2_{-7.5}^{+1.5}$  days and  $z = 0.40_{-0.08}^{+0.13}$ , respectively. The same explosion date as FRB 151230 is included in both of the possible templates with  $s = 0.8$  and  $0.6$ .

### 3.2 Multiwavelength observations and host galaxies

In addition to the multicolor light curves of candidates and the candidate locations in the host galaxies, the multi-wavelength observations and the properties of the host galaxies are useful to constrain the nature of candidates.

Assuming that FRB 151230 is located at the locations of candidates, we estimate the intrinsic radio S/N of FRB 151230 and summarize it in Table 3. Taking into account these locations and the putative intrinsic brightness, FRB 151230 at the location

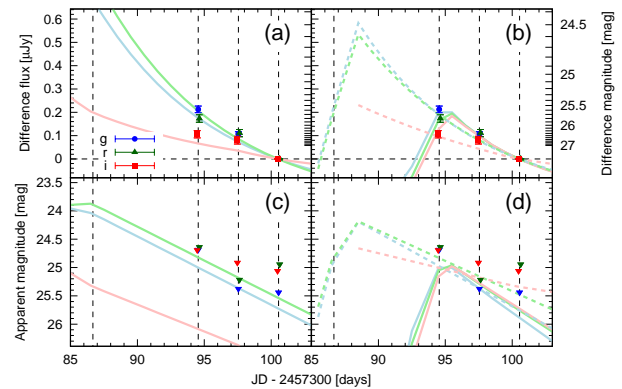


**Fig. 7.** (ab) Comparisons of the difference light curves of Cand-3 and the best-fit RT templates with  $s = 1$  [PS1-11qr, (a)],  $s = 0.8$  [PS1-10ah, dashed in (b)], and  $s = 0.6$  [PS1-10bjp, solid in (b)]. The fluxes are shifted to be zero at the faintest epoch. (cd) Comparisons of the upper limits for the fluxes of Cand-3 in the stacked images and the apparent magnitudes of the best-fit RT templates with  $s = 1$  [PS1-11qr, (c)],  $s = 0.8$  [PS1-10ah, dashed in (d)], and  $s = 0.6$  [PS1-10bjp, solid in (d)].

of Cand-5 can be detected with beam 01 of the receiver at Parkes with an S/N of  $\sim 7$ . On the other hand, FRB 151230 at the location of the other candidates cannot be detected with the other beams. The non-detection of FRB 151230 in the other beams excludes Cand-5 as an optical counterpart to FRB 151230. Here, we assume a Gaussian profile for each feed horn of the multi-beam receiver at Parkes (Manchester et al. 2001).

Bhandari et al. (2018) reported several radio sources detected in the follow-up observations with the Australia Telescope Compact Array (ATCA, Wilson et al. 2011), the Karl G. Jansky Very Large Array (VLA), and the Giant Metrewave Radio Telescope (GMRT, Ananthakrishnan 1995). None of these is located within two times the FWHM of the synthesis beams from the sources detected by VLA and GMRT. On the other hand, Cand-1 and Cand-10 (likely AGN) are located at a distance of about twice the FWHM of the synthesis beam at 5.5 GHz from the sources detected only with ATCA although any association cannot be conclusive because there are other optical sources in the wide elongated synthesis beam of ATCA. Our other candidates are not associated with any radio sources. The radio flux densities at 5.5 GHz and 7.5 GHz are  $22.2 \pm 0.1$  mJy and  $20.2 \pm 0.1$  mJy for Cand-1 and  $0.84 \pm 0.06$  mJy and  $0.62 \pm 0.07$  mJy for Cand-10. The spectral slopes are  $\alpha_{\text{LF}} = -0.31 \pm 0.03$  and  $-0.96 \pm 0.57$  for Cand-1 and Cand-10, respectively. These slopes are consistent with  $\alpha_{\text{LF}}$  of AGN (Planck Collaboration et al. 2016). Additionally, the optical light curves of Cand-1 and Cand-10 are inconsistent with the transient templates. Therefore, if Cand-1 and Cand-10 are associated with the radio sources reported by Bhandari et al. (2018), they are likely to be optical variabilities of AGN. The persistent optical counterparts of the radio sources are described in Appendix 3.

We further compare the candidate locations with the Wide-field Infrared Survey Explorer (WISE) catalog (Mainzer et al. 2011), and find that only the host galaxy of Cand-2 could host a AGN based on the color of  $W1 - W2 \geq 0.8$  mag (Vega, Stern et al. 2012). However, there are multiple galaxies within a resolution element of WISE (Figure 4) and Cand-2 is located off-center of the host galaxy. Thus, Cand-2 is not necessarily the optical variability of an AGN. Furthermore, we check the ROSAT catalog (Boller et al. 2016), the 3XMM-DR7 catalog (Rosen et al. 2016), and the NRAO VLA Sky Survey (NVSS, 1.4 GHz) catalog (Condon et al. 1998) but there are no associated sources with our 13 variable candidates in these catalogs.

Along with the photometric redshifts of the host galaxies, their stellar masses and star formation rates (SFRs) are also derived for the 12 candidates other than Cand-3. The photometric redshifts of the host galaxies of the 11 candidates other than Cand-3 and Cand-6 are consistent with the maximum redshift inferred from the DM of FRB 151230. While the stellar masses of the host galaxies of the 11 candidates other than Cand-2 and Cand-3 are  $\geq 10^9 M_\odot$ , the stellar mass of the host galaxy of Cand-2 is  $8.6 \times 10^7 M_\odot$  comparable with the stellar mass of the host galaxy of FRB 121102 (Bassa et al. 2017; Kokubo et al. 2017; Tendulkar et al. 2017). On the other hand, the SFR of the host galaxy of Cand-2 is  $0.03 M_\odot \text{ yr}^{-1}$  an order of magnitude lower than that of the host galaxy of FRB 121102. The host galaxy of Cand-2 is classified as a star-forming galaxy and it is consistent with the conclusion that Cand-2 is CCSN or RT. The host galaxies of the 11 candidates other than Cand-3 and Cand-5 have the SFR of  $> 10^{-2} M_\odot \text{ yr}^{-1}$  as a median value and are consistent with hosting CCSNe.

#### 4 Testing Type Ia Supernovae as the origin of FRB 151230

The comparisons of the 13 candidates with SN Ia templates give  $Q < 4 \times 10^{-8}$ . Thus, we conclude that all of candidates are inconsistent with SN Ia templates. In this section, we illustrate how the non-detection constrains the association of FRB 151230 with an SN Ia. We adopt the light curve of SNe Ia exploded at Day 0, i.e.,  $t_{\text{exp}} = 0$ , with  $s = 1$  and  $c = 0$ .

Figure 8 shows the difference magnitude with respect to the flux at Day 14. The PSF magnitudes with detection completeness of 50% are also shown. The difference magnitude of SN Ia is brighter for longer time intervals. The 50% completeness magnitude is comparable with the difference magnitude of SN Ia at  $z \sim 0.6$  between Days 8 and 14. Therefore, our analysis can exclude the association of SNe Ia with  $t_{\text{exp}} = 0$  at  $z \leq 0.6$  with FRB 151230. On the other hand, the DM of FRB 151230 puts an upper limit on its redshift of  $z \sim 0.8$  assuming an average line of sight in the Universe (Bhandari et al. 2018). Our results leave room for SNe Ia association with FRB 151230 at

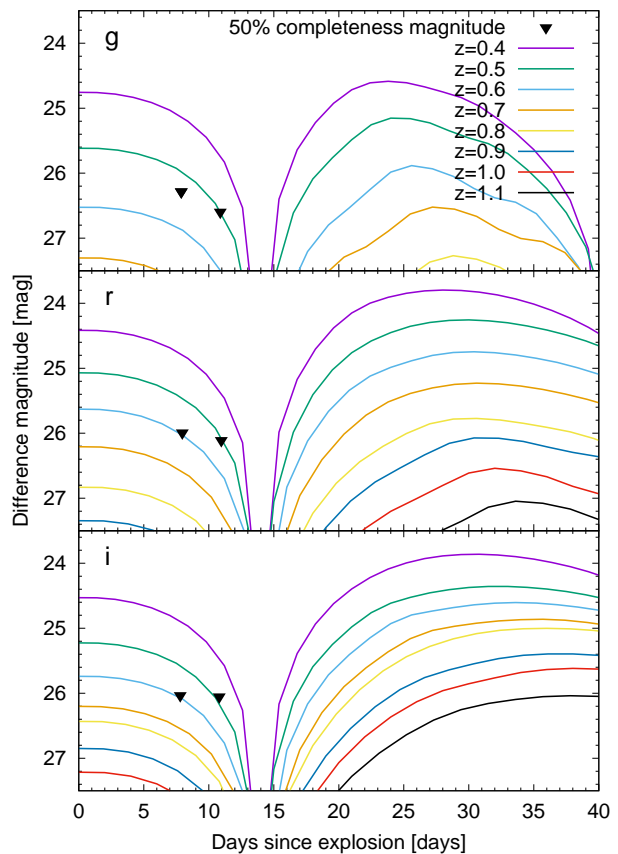


Fig. 8. Magnitude of absolute difference fluxes of SN Ia templates with respect to Day 14. The 50% completeness magnitudes are shown with downward triangles.

$z \sim 0.6 - 0.8$ . In this range, this constraint then corresponds to an upper limit of the DM of the host galaxy of FRB 151230. If an SN Ia is associated with FRB 151230, the DM of the host galaxy of FRB 151230 needs to be less than  $\sim 300 \text{ pc cm}^{-3}$  (McQuinn 2014).

#### 5 Discussion & Conclusion

We performed optical follow-up observations of FRB 151230 using Subaru/HSC on Days 8, 10, and 14 after a realtime alert from the SUPERB collaboration (Bhandari et al. 2018). The survey field covers the localization area of FRB 151230, and the 50% completeness magnitude is 26.5 mag for point sources, which is the deepest among the optical follow-up observations of FRBs covering the entire localization area.

After various sifting and screening techniques are applied and subsequent visual inspection, we find 13 candidates in the localization area of FRB 151230. The properties of 13 candidates are summarized in Table 6. Among them, the association of Cand-5 with FRB 151230 is excluded by the non-detection in the radio of FRB 151230 in the other beams at Parkes. Another 8 candidates are inconsistent with the transient templates and

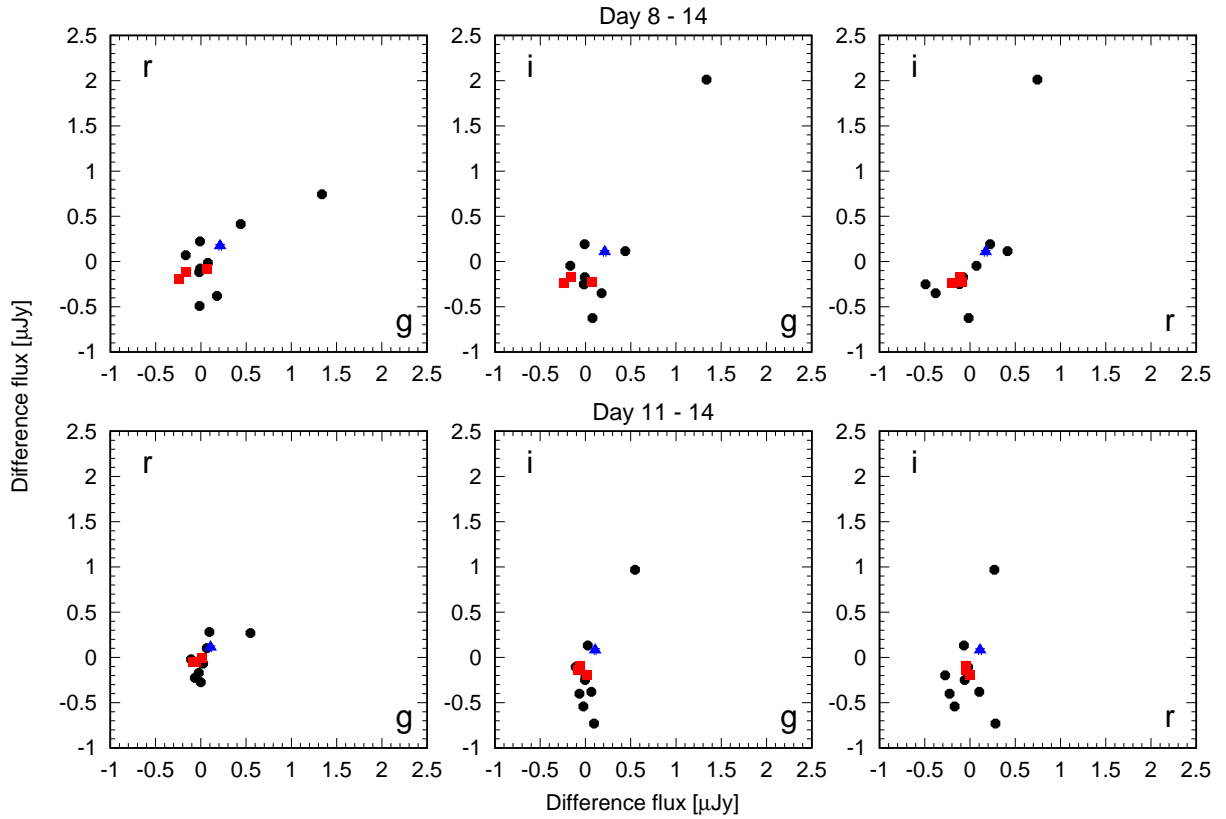


Fig. 9.  $g$ -,  $r$ -, and  $i$ -band difference fluxes of candidates (red: Cand-2, Cand-6, and Cand-11, blue: Cand-3, and black: the others).

are located at the center of extended objects, and thus could be optical variabilities of AGNs. In particular, Cand-1 and Cand-10 are located at a distance of about twice the FWHM from the radio sources detected with ATCA, and the spectral slopes of the radio sources are consistent with that of the AGN. Although the possibility that one of these 8 candidates and the optical variability of AGN are associated with FRB 151230 is not ruled out, it is also possible that all of them are unrelated to FRB 151230 and the association between them and FRB 151230 can not be investigated from our optical follow-up observations. The photometric redshifts of the host galaxies of these 8 candidates are consistent with the maximum redshift inferred from the DM of FRB 151230.

After considering the agreement of light curves fit with known transient templates, the location of candidates in host galaxies, and photometric redshifts, we focus on 3 candidates. The final candidate, Cand-6, is associated with a galaxy with a photometric redshift higher than the maximum redshift estimated from the DM of FRB 151230. They are not prominent in  $g$ -,  $r$ -, and  $i$ -band difference fluxes (Figure 9). Two candidates among the 3 that we deemed to be most interesting are well fitted with transient templates with  $Q > 10^{-4}$ . Their most probable templates are RTs at  $z = 0.60_{-0.23}^{+0.03}$ , SN IIP at  $z = 0.20_{-0.03}^{+0.03}$ , and SNe IIn at  $z = 0.55_{-0.23}^{+0.08}$  for Cand-2, and SNe IIn at  $z = 0.10_{-0.03}^{+0.03}$  for Cand-11. Cand-11 is located at the

center of an extended object and thus could be due to the optical variabilities of AGN. Cand-3 is not well fitted with the transient templates and located off-center of its host galaxy. However, by stretching the RT templates, the multicolor light curves of Cand-3 are reproduced with  $0.15 \leq s \leq 0.8$ . This suggests that Cand-3 is an RT with a rather faint peak and rapid decline. Cand-2 and Cand-3 could have exploded at the same date as FRB 151230, although some theoretical models for FRBs do not necessarily require this. However, we can not conclude their association with FRB 151230.

According to a theoretical estimate with a mock catalog of SNe and observed SN rates (Niino et al. 2014), the number of candidates reproduced with SN templates, i.e., Cand-2, Cand-6, and Cand-11, is consistent with the total SN rate, including SNe Ia and CCSNe. Also, the number density of candidates reproduced with the transient templates inside the localization area of FRB 151230 is roughly consistent with that outside the localization area of FRB 151230 (Appendix 1) and that of SNe detected in a previous study with a time interval of 6 days (Morokuma et al. 2008).

No candidates are reproduced with the SN Ia template. Comparing the 50% completeness magnitude with the difference light curve of SN Ia templates, our observation is sensitive enough to detect SNe Ia with  $t_{\text{exp}} = 0$  at  $z \leq 0.6$ . According to the DM of FRB 151230, this leaves room for an SNe Ia associ-

ation with FRB 151230 only at  $z \sim 0.6 - 0.8$ . In other words, if an SN Ia is associated with FRB 151230, the DM of the host galaxy of FRB 151230 needs to be less than  $\sim 300 \text{ pc cm}^{-3}$ .

Cand-2 and Cand-3 can be well fitted as RTs, of which the volumetric rate is 4 – 7% of the CCSN rate (Drout et al. 2014). While Cand-2 might be an SN IIn according to the  $Q$  values, the multicolor light curves of Cand-3 can be reproduced only with RTs with a faint peak and rapid decline. The light curve of Cand-3 is well reproduced with the stretched RT templates with  $0.15 \leq s \leq 0.8$  with  $Q > 10^{-4}$ . The most probable templates for Cand-3 include the RT templates with the same explosion date as FRB 151230. We compute the expected number of RTs which will be detected coincidentally in the localization area with  $g$ -band differential flux  $> 0.2 \mu\text{Jy}$  in a six-day interval using the method outlined in Niino et al. (2014). We utilize the best-fit template for Cand-3 after stretching, the resultant number of coincident RTs in the localization area is as small as 0.038, and the probability to have this event during the observation is thus 3.6% according to the Poisson distribution. Outside the localization area of FRB 151230, the number of candidates best-fitted with the RT template is 1. These results suggest that the coincident detection of an RT irrelevant to FRB 151230 is relatively unlikely in the localization area. Thus, if Cand-3 is an RT, it may relate to FRB 151230. The volumetric rates of RTs and FRBs are consistent (Drout et al. 2014; Keane & Petroff 2015; Bhandari et al. 2018).

There are two possible mechanisms in the literature for an RT and FRB to be associated; (1) the RT emission from an ultra-stripped Type Ic supernova from a close interacting binary system (Suwa et al. 2015; Tauris et al. 2015; Moriya et al. 2017; Yoshida et al. 2017) and the FRB emission from the interaction between supernova shock and magnetosphere of a neutron star (Egorov & Postnov 2009), and (2) the RT emission from an accretion-induced collapse of the merger remnant of He and CO white dwarfs (Brooks et al. 2017) and the FRB emission from the collapse of a strongly magnetized supermassive rotating neutron star to a black hole immediately after the accretion-induced collapse (Falcke & Rezzolla 2014; Zhang 2014; Moriya 2016). However, there is a major caveat that the RT ejecta can be optically thick at radio frequencies immediately after the explosion and can totally absorb the FRB emission (Connor et al. 2016; Piro 2016; Kashiyama & Murase 2017).

Our observation demonstrates that deep and wide observations detect several unassociated transients in the localization area of FRB. Thus, it is important to establish a method to exclude them. Theoretical studies need to more precisely predict light curve evolution to identify the optical counterparts of FRBs.

The optical observations give a lower limit on the redshift. This is complementary with the upper limit on redshift of FRBs that can be estimated by the DM of FRBs. We encourage rapid

reporting of FRBs, especially those with low DM values, to enable future wide-field optical work aiming at identifying any and all associated emission in this band.

## Acknowledgments

This research has been supported in part by the research grant program of Toyota foundation (D11-R-0830), the natural science grant of the Mitsubishi Foundation, the research grant of the Yamada Science Foundation, World Premier International Research Center Initiative, MEXT, Japan, and by JSPS KAKENHI Grant Numbers JP15H02075, JP15H05440, JP15K05018, JP16H02158, JP17H06362, JP17H06363, JP17K14255, JP18K03692. EP receives funding from the European Research Council under the European Union Seventh Framework Programme (FP/2007-2013) / ERC Grant Agreement n. 617199. We thank the LSST Project for making their code available as free software at <http://dm.lsstcorp.org>. Funding for SDSS-III has been provided by the Alfred P. Sloan Foundation, the Participating Institutions, the National Science Foundation, and the U.S. Department of Energy Office of Science. The SDSS-III web site is <http://www.sdss3.org/>. SDSS-III is managed by the Astrophysical Research Consortium for the Participating Institutions of the SDSS-III Collaboration including the University of Arizona, the Brazilian Participation Group, Brookhaven National Laboratory, Carnegie Mellon University, University of Florida, the French Participation Group, the German Participation Group, Harvard University, the Instituto de Astrofísica de Canarias, the Michigan State/Notre Dame/JINA Participation Group, Johns Hopkins University, Lawrence Berkeley National Laboratory, Max Planck Institute for Astrophysics, Max Planck Institute for Extraterrestrial Physics, New Mexico State University, New York University, Ohio State University, Pennsylvania State University, University of Portsmouth, Princeton University, the Spanish Participation Group, University of Tokyo, University of Utah, Vanderbilt University, University of Virginia, University of Washington, and Yale University.

## Appendix 1 Transients outside the localization area of FRB 151230

As the field of view of HSC is 9 times wider than a circle with a radius of 15 arcmin, i.e., the localization area of FRB 151230 adopted in this paper, although the depth outside the localization area is 0.34 mag shallower than that inside the localization area. Thus, we have a large sample of candidates being irrelevant to FRB 151230, which can be a control sample. We perform the visual inspection and the light curve fitting for the 490 candidates outside the localization area of FRB 151230. If the photometric redshift of the host galaxy is available, only the templates in the 95% probability are allowed. As a result, 19 visually-selected candidates<sup>5</sup> are fitted well with the transient templates (Table 7 and Figure 10) with the  $Q$  values better than the best-fit template for Cand-3, i.e.,  $Q > 2 \times 10^{-6}$ . Taking into account the wide area and the shallow depth outside the localization area of FRB 151230, the number density of candidates reproduced with

<sup>5</sup> The number of candidates reproduced with the transient templates is 17 if we adopt the criterion of  $Q > 10^{-4}$ .

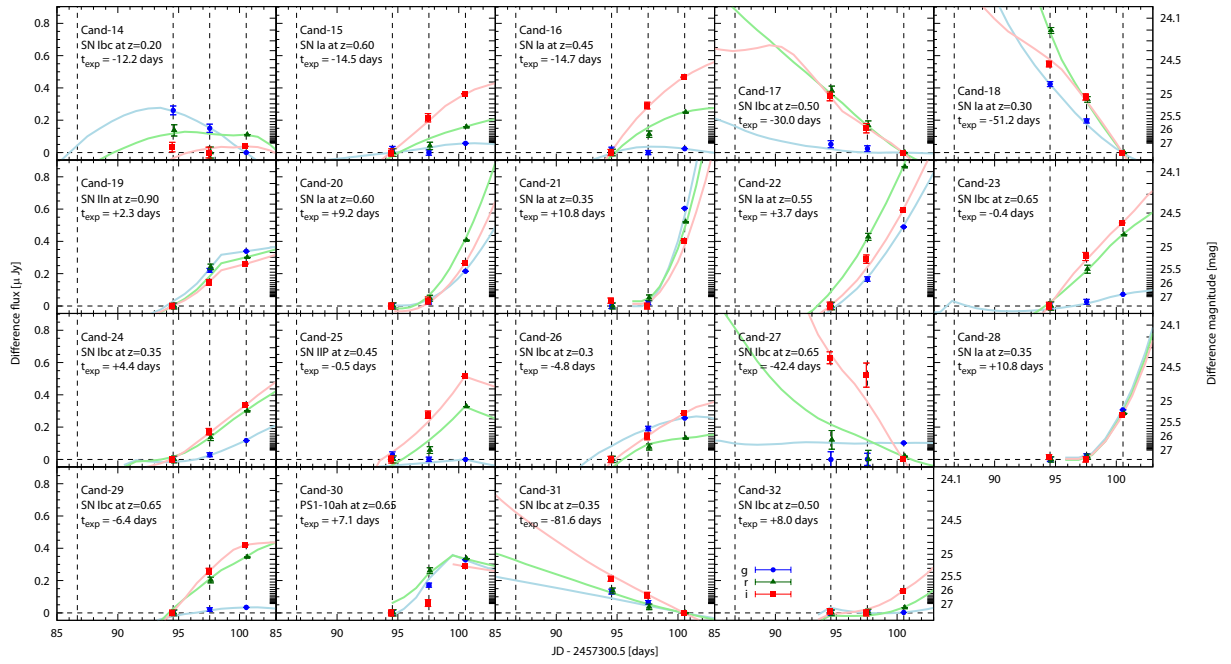


**Fig. 10.** Comparisons of the difference light curves of the transients outside the localization area of FRB 151230 and the best-fit templates. The fluxes are shifted to be zero at the faintest epoch.

the transient templates is roughly consistent with that of candidates inside the localization area of FRB 151230. The best-fit templates are SNe Ia for 7 candidates, CCSNe for 11 candidates, and an RT for 1 candidate. Considering the small number statistics, the ratio of the numbers of the candidates consistent with RT templates to those with CCSN templates is consistent with the ratio of RTs to CCSNe (4% – 7%, Drout et al. 2014).

## Appendix 2 Light curve fitting

For the light curve fitting, we adopt templates of SNe Ia (Hsiao et al. 2007), CCSNe (Nugent et al. 2002), and RTs (Drout et al. 2014). In order to take into account intrinsic variations, we allow variations of several parameters; stretch  $s$ , color  $c$ , and intrinsic variation  $I$  for the SN Ia templates, and peak absolute  $B$ -band magnitude  $M_B$  and extinction in the host galaxy for the CCSN and RT templates. The peak absolute  $B$ -band magnitude  $M_B$  of the SN Ia templates is derived with equation (4) in Barbary et al. (2012). The host galaxy extinction for the CCSN and RT templates is characterized with the color excess  $E_{B-V, \text{host}}$  with a range of 0.0 to 1.0, and the extinction curve of the host galaxy is assumed to be the same as in our Galaxy (Pei 1992). While we adopt the peak magnitudes of the observed RTs with assuming a variation of  $\pm 1$  mag, the average and variation of other parameters are taken from Barbary et al. (2012) for SNe Ia and Dahlen et al. (2012) for CCSNe. The adopted templates and the range of variation are summarized in Table 8.

Template light curves are derived with interpolating or extrapolating the spectral energy distribution for various redshift

from  $z = 0$  to  $z = 4$  for SNe IIn or from  $z = 0$  to  $z = 2$  for other transients with  $\Delta z = 0.05$  as done in Okumura et al. (2014); Niino et al. (2014). We force the template to have the information of the  $g$ -,  $r$ -, and  $i$ -bands at least in an epoch and to have the information of at least 1 band in more than 1 epoch. The explosion date  $t_{\text{exp}}$  of templates since the occurrence time of FRB 151230 are varied with  $\Delta t_{\text{exp}} = 1$  day at  $t_{\text{exp}} \leq 11$  day in the observer frame. With the derived template light curves, we calculate fluxes on Days 8, 11, and 14 and difference fluxes between Days 8 and 14 and between Days 11 and 14.

We expediently judge the agreement of light curves of candidates and templates with the use of the  $Q$  value of chi square statistics as a guide. The chi square is defined as

$$\chi^2 = \sum_{\text{difference}} \frac{(f_{d,\text{obs}} - f_{d,\text{temp}})^2}{\sigma_{d,\text{obs}}^2} \times \{1 - \Theta(3\sigma_{d,\text{obs}} - |f_{d,\text{obs}}|) \Theta(3\sigma_{d,\text{obs}} - |f_{d,\text{temp}}|)\} + \sum_{\text{stacked}} \frac{(f_{s,\text{obs}} - f_{s,\text{temp}})^2}{\sigma_{s,\text{obs}}^2} \Theta(f_{s,\text{temp}} - f_{s,\text{obs}}), \quad (\text{A1})$$

where  $f_{i,\text{obs}}$ ,  $f_{i,\text{temp}}$ , and  $\sigma_{i,\text{obs}}$  are the observed flux, the template flux, and the observed standard deviation, respectively. The suffix  $i$  represents  $s$  for the stacked images and  $d$  for the difference images. The Heaviside function  $\Theta(x)$  is defined to be  $\Theta(x) = 1$  for  $x > 0$  and 0 otherwise. The number of observations that are used for the estimation of  $\chi^2$  is

$$n_{\text{obs}} = \sum_{\text{difference}} \{1 - \Theta(3\sigma_{d,\text{obs}} - |f_{d,\text{obs}}|) \Theta(3\sigma_{d,\text{obs}} - |f_{d,\text{temp}}|)\} + \sum_{\text{stacked}} \Theta(f_{s,\text{temp}} - f_{s,\text{obs}}). \quad (\text{A2})$$

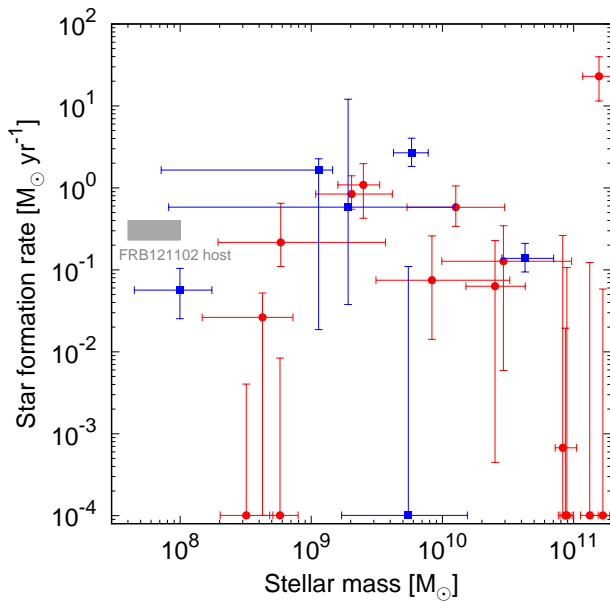


**Fig. 11.** Stellar masses and star formation rates of optical counterparts of radio sources detected with VLA and GMRT (points) and of the host galaxy of FRB 121102 (shaded region, Kokubo et al. 2017; Bassa et al. 2017; Tendulkar et al. 2017). The objects with  $W1 - W2 \geq +0.8$  mag and  $W1 - W2 \leq +0.8$  mag are shown in blue squares and red circles, respectively. The error bars represent the 68% probability.

A degree of freedom of the chi square statistics is the difference between the numbers of independent observations and independent parameters. However, an identification of the independent parameters requires great care and our aim is only to constrain possible templates. Thus we conservatively set the degree of freedom  $\nu$  as  $(n_{\text{obs}} - 1)$  because  $t_{\text{exp}}$  is obviously independent on the other parameters related to the properties of transients.

### Appendix 3 Persistent optical counterparts of radio sources

The radio follow-up observations of FRB 151230 with VLA and GMRT detect 32 independent radio sources (Bhandari et al. 2018). Among them, 22 radio sources have extended optical counterparts within the FWHM of the synthesis beams in the *gri* images obtained on Day 10 which have the best seeing. Here, we adopt the position measured with GMRT if a source is detected with both of VLA and GMRT because GMRT has a higher spatial resolution than VLA. For these optical counterparts, the stellar masses and the SFR are derived using the photometric redshift code and summarized in Figure 11. Also, we compare the locations of radio sources having optical counterparts with the WISE catalog and identify the sources being likely to host a AGN. There are no radio source hosted in a galaxy identical with the host galaxy of FRB 121102 in terms of the stellar mass and SFR, and some of the radio sources could be

emissions from AGNs according to the WISE color of the host galaxies. Further observations are required to conclude whether the radio sources are associated with FRB 151230 or not.

### References

- Akiyama, K., & Johnson, M. D. 2016, *ApJL*, 824, L3  
 Alard, C., & Lupton, R. H. 1998, *ApJ*, 503, 325  
 Ananthakrishnan, S. 1995, *Journal of Astrophysics and Astronomy Supplement*, 16, 427  
 Axelrod, T., Kantor, J., Lupton, R. H., & Pierfederici, F. 2010, in *Society of Photo-Optical Instrumentation Engineers (SPIE) Conference Series*, Vol. 7740, Society of Photo-Optical Instrumentation Engineers (SPIE) Conference Series, 15  
 Bannister, K. W., & Madsen, G. J. 2014, *MNRAS*, 440, 353  
 Bannister, K. W., et al. 2017, *ApJL*, 841, L12  
 Barbary, K., et al. 2012, *ApJ*, 745, 31  
 Bassa, C. G., et al. 2016, *MNRAS*, 463, L36  
 —. 2017, *ApJL*, 843, L8  
 Bhandari, S., et al. 2018, *MNRAS*, 475, 1427  
 Boller, T., Freyberg, M. J., Trümper, J., Haberl, F., Voges, W., & Nandra, K. 2016, *A&A*, 588, A103  
 Bosch, J., et al. 2017, *ArXiv e-prints*, arXiv:1705.06766  
 Brooks, J., Schwab, J., Bildsten, L., Quataert, E., Paxton, B., Blinnikov, S., & Sorokina, E. 2017, *ApJ*, 850, 127  
 Caleb, M., et al. 2017, *MNRAS*, 468, 3746  
 Chambers, K. C., et al. 2016, *ArXiv e-prints*, arXiv:1612.05560  
 Champion, D. J., et al. 2016, *MNRAS*, 460, L30  
 Chatterjee, S., et al. 2017, *Nature*, 541, 58  
 Condon, J. J., Cotton, W. D., Greisen, E. W., Yin, Q. F., Perley, R. A., Taylor, G. B., & Broderick, J. J. 1998, *AJ*, 115, 1693  
 Connor, L., Sievers, J., & Pen, U.-L. 2016, *MNRAS*, 458, L19  
 Cordes, J. M., & Wasserman, I. 2016, *MNRAS*, 457, 232  
 Dahlen, T., Strolger, L.-G., Riess, A. G., Mattila, S., Kankare, E., & Mobasher, B. 2012, *ApJ*, 757, 70  
 Drout, M. R., et al. 2014, *ApJ*, 794, 23  
 Egorov, A. E., & Postnov, K. A. 2009, *Astronomy Letters*, 35, 241  
 Falcke, H., & Rezzolla, L. 2014, *A&A*, 562, A137  
 Hsiao, E. Y., Conley, A., Howell, D. A., Sullivan, M., Pritchett, C. J., Carlberg, R. G., Nugent, P. E., & Phillips, M. M. 2007, *ApJ*, 663, 1187  
 Ivezić, Z., Tyson, J. A., Allsman, R., Andrew, J., Angel, R., & for the LSST Collaboration. 2008, *ArXiv e-prints*, arXiv:0805.2366  
 Johnston, S., et al. 2017, *MNRAS*, 465, 2143  
 Jurić, M., et al. 2015, *ArXiv e-prints*, arXiv:1512.07914  
 Kashiyama, K., Ioka, K., & Mészáros, P. 2013, *ApJL*, 776, L39  
 Kashiyama, K., & Murase, K. 2017, *ApJL*, 839, L3  
 Keane, E. F., & Petroff, E. 2015, *MNRAS*, 447, 2852  
 Keane, E. F., Stappers, B. W., Kramer, M., & Lyne, A. G. 2012, *MNRAS*, 425, L71  
 Keane, E. F., et al. 2016, *Nature*, 530, 453  
 —. 2018, *MNRAS*, 473, 116  
 Kokubo, M., et al. 2017, *ApJ*, 844, 95  
 Lorimer, D. R., Bailes, M., McLaughlin, M. A., Narkevic, D. J., & Crawford, F. 2007, *Science*, 318, 777  
 Macquart, J.-P., & Ekers, R. D. 2018, *MNRAS*, 474, 1900  
 Mainzer, A., et al. 2011, *ApJ*, 731, 53

Manchester, R. N., et al. 2001, MNRAS, 328, 17  
 Marcote, B., et al. 2017, ApJL, 834, L8  
 Masui, K., et al. 2015, Nature, 528, 523  
 McQuinn, M. 2014, ApJL, 780, L33  
 Miyazaki, S., et al. 2012, in Society of Photo-Optical Instrumentation Engineers (SPIE) Conference Series, Vol. 8446, Society of Photo-Optical Instrumentation Engineers (SPIE) Conference Series, 0  
 Miyazaki, S., et al. 2018, PASJ, 70, S1  
 Morii, M., et al. 2016, PASJ, 68, 104  
 Moriya, T. J. 2016, ApJL, 830, L38  
 Moriya, T. J., et al. 2017, MNRAS, 466, 2085  
 Morokuma, T., et al. 2008, ApJ, 676, 163  
 Niino, Y., Totani, T., & Okumura, J. E. 2014, PASJ, 66, L9  
 Nugent, P., Kim, A., & Perlmutter, S. 2002, PASP, 114, 803  
 Okumura, J. E., et al. 2014, PASJ, 66, 49  
 Pei, Y. C. 1992, ApJ, 395, 130  
 Pen, U.-L., & Connor, L. 2015, ApJ, 807, 179  
 Petroff, E., et al. 2015a, MNRAS, 454, 457  
 —. 2015b, MNRAS, 447, 246  
 —. 2016, PASA, 33, e045  
 Pian, E., et al. 2017, Nature, 551, 67  
 Piro, A. L. 2016, ApJL, 824, L32  
 Planck Collaboration, et al. 2016, A&A, 596, A106  
 Ravi, V., Shannon, R. M., & Jameson, A. 2015, ApJL, 799, L5  
 Ravi, V., et al. 2016, Science, 354, 1249  
 Rosen, S. R., et al. 2016, A&A, 590, A1  
 Schlafly, E. F., & Finkbeiner, D. P. 2011, ApJ, 737, 103  
 Spitler, L. G., et al. 2014, ApJ, 790, 101  
 —. 2016, Nature, 531, 202  
 Stern, D., et al. 2012, ApJ, 753, 30  
 Suwa, Y., Yoshida, T., Shibata, M., Umeda, H., & Takahashi, K. 2015, MNRAS, 454, 3073  
 Tanaka, M. 2015, ApJ, 801, 20  
 Tauris, T. M., Langer, N., & Podsiadlowski, P. 2015, MNRAS, 451, 2123  
 Tendulkar, S. P., et al. 2017, ApJL, 834, L7  
 Thornton, D., et al. 2013, Science, 341, 53  
 Tominaga, N., et al. 2018, PASJ, arXiv:1710.05865  
 Totani, T. 2013, PASJ, 65, L12  
 Utsumi, Y., et al. 2017, PASJ, 69, 101  
 —. 2018, PASJ, 70, 1  
 Vieyro, F. L., Romero, G. E., Bosch-Ramon, V., Marcote, B., & del Valle, M. V. 2017, A&A, 602, A64  
 Williams, P. K. G., & Berger, E. 2016, ApJL, 821, L22  
 Wilson, W. E., et al. 2011, MNRAS, 416, 832  
 Yoshida, T., Suwa, Y., Umeda, H., Shibata, M., & Takahashi, K. 2017, MNRAS, 471, 4275  
 Zhang, B. 2014, ApJL, 780, L21

**Table 1.** Observations with Subaru/Hyper Suprime-Cam.

UT	Epoch	Filter	Exposure time (s)	Seeing <sup>a</sup> (arcsec)	Limiting magnitude <sup>b</sup> (mag)
2016-01-07	Day 8	<i>g</i>	3150	1.44	26.4
2016-01-07	Day 8	<i>r</i>	4200	1.26	26.3
2016-01-07	Day 8	<i>i</i>	4200	0.91	26.5
2016-01-10	Day 11	<i>g</i>	3600	0.83	27.3
2016-01-10	Day 11	<i>r</i>	4080	0.68	27.3
2016-01-10	Day 11	<i>i</i>	3600	0.70	26.6
2016-01-13	Day 14	<i>g</i>	3600	1.31	26.5
2016-01-13	Day 14	<i>r</i>	3600	1.43	26.0
2016-01-13	Day 14	<i>i</i>	3600	0.81	26.4

<sup>a</sup>Full width at half maximum in the stacked images.<sup>b</sup>5 $\sigma$  limiting magnitude with aperture diameter of twice of FWHM of seeing.**Table 2.** Information regarding difference images.

Epoch	Filter	PSF size <sup>a</sup> (arcsec)	Limiting magnitude <sup>b</sup> (mag)	50% completeness magnitude <sup>c</sup> (mag)	50% completeness magnitude <sup>d</sup> (mag)
Day 8 – 14	<i>g</i>	1.44	26.3	26.6	26.3
Day 8 – 14	<i>r</i>	1.44	26.0	26.2	26.0
Day 8 – 14	<i>i</i>	0.91	26.2	26.3	26.0
Day 11 – 14	<i>g</i>	1.31	26.7	26.9	26.6
Day 11 – 14	<i>r</i>	1.43	26.2	26.4	26.1
Day 11 – 14	<i>i</i>	0.81	26.3	26.3	26.1

<sup>a</sup>Full width at half maximum in the difference images.<sup>b</sup>5 $\sigma$  limiting magnitude with aperture diameter of twice of FWHM of PSF.<sup>c</sup>PSF magnitude with the detection completeness of 50% before the source screening.<sup>d</sup>PSF magnitude with the detection completeness of 50% after the source screening.

Table 3. Candidate information.

Name				
Separation <sup>a</sup> (arcmin)	Separation <sup>b</sup> (arcsec)	Radio S/N <sup>c</sup>	RA	Dec
Epoch	<i>g</i> ( $\mu$ Jy)		<i>r</i> ( $\mu$ Jy)	<i>i</i> ( $\mu$ Jy)
Cand-1				
13.92	0.12	250	09:40:10.67	-03:36:56.4
Day 8	+9.515 $\pm$ 0.015 <sup>d</sup>		+16.574 $\pm$ 0.019 <sup>d</sup>	+15.717 $\pm$ 0.017 <sup>d</sup>
Day 11	+5.607 $\pm$ 0.009 <sup>d</sup>		+8.410 $\pm$ 0.010 <sup>d</sup>	+11.845 $\pm$ 0.016 <sup>d</sup>
Day 14	+8.760 $\pm$ 0.012 <sup>d</sup>		+17.617 $\pm$ 0.019 <sup>d</sup>	+13.405 $\pm$ 0.017 <sup>d</sup>
Day 8 – Day 14	-0.167 $\pm$ 0.016		+0.070 $\pm$ 0.019	< +0.055
Day 11 – Day 14	-0.108 $\pm$ 0.012		< +0.054	-0.107 $\pm$ 0.018
Cand-2				
6.24	1.05	29	09:40:29.18	-03:30:32.2
Day 8	+0.454 $\pm$ 0.012 <sup>d</sup>		+0.559 $\pm$ 0.015 <sup>d</sup>	+0.605 $\pm$ 0.014 <sup>d</sup>
Day 11	+0.450 $\pm$ 0.007 <sup>d</sup>		+0.460 $\pm$ 0.007 <sup>d</sup>	+0.556 $\pm$ 0.013 <sup>d</sup>
Day 14	+0.596 $\pm$ 0.010 <sup>d</sup>		+0.717 $\pm$ 0.015 <sup>d</sup>	+0.697 $\pm$ 0.016 <sup>d</sup>
Day 8 – Day 14	-0.160 $\pm$ 0.013		-0.114 $\pm$ 0.016	-0.167 $\pm$ 0.015
Day 11 – Day 14	-0.056 $\pm$ 0.010		< +0.045	-0.090 $\pm$ 0.017
Cand-3				
10.15	0.43	71	09:40:11.07	-03:29:59.4
Day 8	+0.486 $\pm$ 0.014 <sup>d</sup>		+0.507 $\pm$ 0.016 <sup>d</sup>	+0.483 $\pm$ 0.015 <sup>d</sup>
Day 11	+0.257 $\pm$ 0.007 <sup>d</sup>		+0.298 $\pm$ 0.008 <sup>d</sup>	+0.393 $\pm$ 0.014 <sup>d</sup>
Day 14	+0.242 $\pm$ 0.010 <sup>d</sup>		+0.383 $\pm$ 0.016 <sup>d</sup>	+0.344 $\pm$ 0.015 <sup>d</sup>
Day 8 – Day 14	+0.212 $\pm$ 0.014		+0.173 $\pm$ 0.016	+0.106 $\pm$ 0.016
Day 11 – Day 14	+0.107 $\pm$ 0.010		+0.111 $\pm$ 0.015	+0.080 $\pm$ 0.016
Cand-4				
10.08	0.05	70	09:40:10.39	-03:29:02.1
Day 8	+4.365 $\pm$ 0.015 <sup>d</sup>		+11.005 $\pm$ 0.017 <sup>d</sup>	+13.500 $\pm$ 0.016 <sup>d</sup>
Day 11	+2.552 $\pm$ 0.008 <sup>d</sup>		+6.310 $\pm$ 0.010 <sup>d</sup>	+10.800 $\pm$ 0.015 <sup>d</sup>
Day 14	+3.897 $\pm$ 0.012 <sup>d</sup>		+11.718 $\pm$ 0.017 <sup>d</sup>	+11.945 $\pm$ 0.018 <sup>d</sup>
Day 8 – Day 14	< +0.046		-0.077 $\pm$ 0.018	-0.173 $\pm$ 0.017
Day 11 – Day 14	< +0.035		-0.059 $\pm$ 0.017	-0.249 $\pm$ 0.019
Cand-5				
13.04	0.13	180	09:39:57.85	-03:26:25.3
Day 8	+8.552 $\pm$ 0.015 <sup>d</sup>		+19.262 $\pm$ 0.018 <sup>d</sup>	+24.074 $\pm$ 0.018 <sup>d</sup>
Day 11	+6.213 $\pm$ 0.009 <sup>d</sup>		+12.303 $\pm$ 0.011 <sup>d</sup>	+20.053 $\pm$ 0.017 <sup>d</sup>
Day 14	+8.361 $\pm$ 0.013 <sup>d</sup>		+20.372 $\pm$ 0.020 <sup>d</sup>	+22.062 $\pm$ 0.019 <sup>d</sup>
Day 8 – Day 14	< +0.046		-0.491 $\pm$ 0.021	-0.252 $\pm$ 0.019
Day 11 – Day 14	-0.066 $\pm$ 0.013		-0.226 $\pm$ 0.020	-0.401 $\pm$ 0.021
Cand-6				
11.43	0.15	100	09:40:11.61	-03:20:51.9
Day 8	+1.308 $\pm$ 0.014 <sup>d</sup>		+1.108 $\pm$ 0.016 <sup>d</sup>	+1.035 $\pm$ 0.014 <sup>d</sup>
Day 11	+0.926 $\pm$ 0.008 <sup>d</sup>		+0.790 $\pm$ 0.008 <sup>d</sup>	+0.910 $\pm$ 0.013 <sup>d</sup>
Day 14	+1.387 $\pm$ 0.011 <sup>d</sup>		+1.452 $\pm$ 0.017 <sup>d</sup>	+1.152 $\pm$ 0.016 <sup>d</sup>
Day 8 – Day 14	-0.243 $\pm$ 0.014		-0.197 $\pm$ 0.017	-0.240 $\pm$ 0.015
Day 11 – Day 14	-0.086 $\pm$ 0.011		< +0.050	-0.136 $\pm$ 0.017
Cand-7				

Table 3. (Continued)

Name	Separation <sup>a</sup> (arcmin)	Separation <sup>b</sup> (arcsec)	RA	Dec
Epoch		<i>g</i> ( $\mu$ Jy)	<i>r</i> ( $\mu$ Jy)	<i>i</i> ( $\mu$ Jy)
8.44	0.01	46	09:40:19.25	-03:23:35.5
Day 8		$+9.660 \pm 0.015^d$	$+20.887 \pm 0.018^d$	$+27.563 \pm 0.018^d$
Day 11		$+6.936 \pm 0.009^d$	$+13.976 \pm 0.011^d$	$+23.124 \pm 0.017^d$
Day 14		$+8.744 \pm 0.013^d$	$+21.718 \pm 0.020^d$	$+25.308 \pm 0.020^d$
Day 8 - Day 14		$+0.439 \pm 0.016$	$+0.414 \pm 0.020$	$+0.114 \pm 0.019$
Day 11 - Day 14		$+0.066 \pm 0.013$	$+0.102 \pm 0.019$	$-0.380 \pm 0.021$
Cand-8				
8.68	0.03	48	09:40:18.22	-03:23:35.1
Day 8		$+9.394 \pm 0.016^d$	$+26.611 \pm 0.020^d$	$+37.181 \pm 0.020^d$
Day 11		$+6.789 \pm 0.009^d$	$+18.755 \pm 0.013^d$	$+31.848 \pm 0.020^d$
Day 14		$+8.917 \pm 0.013^d$	$+28.091 \pm 0.021^d$	$+34.622 \pm 0.023^d$
Day 8 - Day 14		$+0.077 \pm 0.016$	$< +0.064$	$-0.625 \pm 0.021$
Day 11 - Day 14		$+0.094 \pm 0.013$	$+0.281 \pm 0.020$	$-0.731 \pm 0.024$
Cand-9				
12.54	0.10	150	09:40:02.18	-03:23:16.7
Day 8		$+5.229 \pm 0.015^d$	$+12.062 \pm 0.018^d$	$+15.041 \pm 0.016^d$
Day 11		$+3.852 \pm 0.008^d$	$+8.492 \pm 0.010^d$	$+12.662 \pm 0.015^d$
Day 14		$+4.915 \pm 0.012^d$	$+12.842 \pm 0.018^d$	$+13.898 \pm 0.018^d$
Day 8 - Day 14		$< +0.045$	$+0.223 \pm 0.018$	$+0.191 \pm 0.017$
Day 11 - Day 14		$< +0.037$	$-0.067 \pm 0.018$	$+0.132 \pm 0.019$
Cand-10				
10.59	0.03	81	09:41:23.97	-03:20:44.9
Day 8		$+7.762 \pm 0.015^d$	$+12.770 \pm 0.017^d$	$+14.591 \pm 0.016^d$
Day 11		$+5.266 \pm 0.008^d$	$+8.069 \pm 0.010^d$	$+11.342 \pm 0.014^d$
Day 14		$+7.222 \pm 0.012^d$	$+14.180 \pm 0.018^d$	$+12.727 \pm 0.017^d$
Day 8 - Day 14		$+0.178 \pm 0.015$	$-0.380 \pm 0.018$	$-0.350 \pm 0.017$
Day 11 - Day 14		$< +0.036$	$-0.275 \pm 0.018$	$-0.198 \pm 0.018$
Cand-11				
10.55	0.06	80	09:41:26.72	-03:21:52.2
Day 8		$+7.634 \pm 0.014^d$	$+11.339 \pm 0.016^d$	$+11.362 \pm 0.015^d$
Day 11		$+4.762 \pm 0.008^d$	$+6.245 \pm 0.009^d$	$+8.653 \pm 0.014^d$
Day 14		$+7.136 \pm 0.012^d$	$+12.607 \pm 0.017^d$	$+10.132 \pm 0.017^d$
Day 8 - Day 14		$+0.071 \pm 0.015$	$-0.084 \pm 0.018$	$-0.227 \pm 0.016$
Day 11 - Day 14		$< +0.037$	$< +0.051$	$-0.188 \pm 0.018$
Cand-12				
10.68	0.24	83	09:41:12.99	-03:18:04.8
Day 8		$+17.315 \pm 0.017^d$	$+32.989 \pm 0.020^d$	$+37.663 \pm 0.020^d$
Day 11		$+10.673 \pm 0.010^d$	$+19.520 \pm 0.012^d$	$+28.782 \pm 0.018^d$
Day 14		$+14.755 \pm 0.013^d$	$+33.926 \pm 0.020^d$	$+31.625 \pm 0.021^d$
Day 8 - Day 14		$+1.338 \pm 0.017$	$+0.744 \pm 0.021$	$+2.011 \pm 0.021$
Day 11 - Day 14		$+0.549 \pm 0.013$	$+0.270 \pm 0.020$	$+0.969 \pm 0.022$
Cand-13				
8.84	0.19	50	09:40:30.93	-03:19:38.0
Day 8		$+8.246 \pm 0.014^d$	$+25.759 \pm 0.018^d$	$+37.745 \pm 0.020^d$

**Table 3.** (Continued)

Name	Separation <sup>a</sup> (arcmin)	Separation <sup>b</sup> (arcsec)	RA	Dec
Epoch	<i>g</i> ( $\mu$ Jy)	<i>r</i> ( $\mu$ Jy)	<i>i</i> ( $\mu$ Jy)	
Day 11	$+4.469 \pm 0.008^d$	$+14.175 \pm 0.011^d$	$+30.174 \pm 0.018^d$	
Day 14	$+7.466 \pm 0.012^d$	$+28.891 \pm 0.020^d$	$+34.284 \pm 0.021^d$	
Day 8 – Day 14	$< +0.044$	$-0.117 \pm 0.020$	$-0.250 \pm 0.021$	
Day 11 – Day 14	$< +0.035$	$-0.170 \pm 0.019$	$-0.542 \pm 0.022$	

<sup>a</sup>Separation from the center of the localization area of FRB 151230.<sup>b</sup>Separation from the objects in the stacked images or the objects in the PS1 catalog.<sup>c</sup>Intrinsic radio S/N of FRB 151230 at the candidate location.<sup>d</sup>Upper limits for the fluxes of the candidates.**Table 4.** Templates fitting the difference light curves of candidates.

Name (photometric redshift)						
SN Type	Number <sup>a</sup>	Redshift	$t_{\text{exp}}$	$E_{B-V, \text{host}}$	$M_B$	$Q$ value
Cand-2 (photo- $z = 0.18^{+0.46}_{-0.15}$ )						
PS1-10ah <sup>b</sup>	30	$0.60^{+0.03}_{-0.23}$	$+7.2^{+1.1}_{-0.5}$	$0.00^{+0.24}_{-0.00}$	$-16.78^{+0.18}_{-0.13}$	$2.1 \times 10^{-4} - 2.1 \times 10^{-2}$
PS1-10bjp	34	$0.55^{+0.08}_{-0.18}$	$+7.3^{+1.0}_{-0.6}$	$0.20^{+0.23}_{-0.20}$	$-17.20^{+0.03}_{-0.03}$	$2.5 \times 10^{-4} - 1.4 \times 10^{-2}$
Nugent IIn	116	$0.55^{+0.08}_{-0.23}$	$+3.9^{+2.1}_{-4.2}$	$0.14^{+0.31}_{-0.14}$	$-16.96^{+0.03}_{-0.38}$	$2.2 \times 10^{-4} - 1.0 \times 10^{-2}$
Nugent IIP	1	$0.20^{+0.03}_{-0.03}$	$+5.0^{+0.5}_{-0.5}$	$0.05^{+0.01}_{-0.05}$	$-14.41^{+0.03}_{-0.03}$	$2.1 \times 10^{-4}$
Cand-3						
PS1-11qr <sup>b</sup>	9	$0.60^{+0.03}_{-0.13}$	$-12.8^{+2.8}_{-0.5}$	$0.00^{+0.11}_{-0.00}$	$-18.13^{+0.13}_{-0.08}$	$2.2 \times 10^{-8} - 2.2 \times 10^{-6}$
PS1-12brf	1	$0.65^{+0.03}_{-0.03}$	$-2.5^{+0.5}_{-0.5}$	$0.00^{+0.01}_{-0.00}$	$-17.94^{+0.03}_{-0.03}$	$2.3 \times 10^{-8}$
Cand-6 (photo- $z = 1.44^{+0.46}_{-0.27}$ )						
Nugent IIn <sup>b</sup>	29	$1.25^{+0.48}_{-0.08}$	$+0.8^{+1.1}_{-2.4}$	$0.00^{+0.01}_{-0.00}$	$-18.71^{+0.23}_{-0.78}$	$6.7 \times 10^{-6} - 2.5 \times 10^{-4}$
Cand-11 (photo- $z = 0.19^{+0.07}_{-0.15}$ )						
Nugent IIn <sup>b</sup>	8	$0.10^{+0.03}_{-0.03}$	$-6.3^{+0.5}_{-0.5}$	$0.57^{+0.07}_{-0.57}$	$-16.96^{+0.03}_{-0.03}$	$1.5 \times 10^{-4} - 3.0 \times 10^{-3}$

<sup>a</sup>The number of templates fitting the multicolor light curves of candidates.<sup>b</sup>The best-fit template.**Table 5.** Templates fitting the difference light curve of Cand-3 stretching the RT templates.

Stretch						
SN Type	Number <sup>a</sup>	Redshift	$t_{\text{exp}}$	$E_{B-V, \text{host}}$	$M_B$	$Q$ value
$s = 0.8$						
PS1-10ah <sup>b</sup>	45	$0.20^{+0.03}_{-0.03}$	$-1.4^{+7.5}_{-2.5}$	$0.20^{+0.18}_{-0.16}$	$-16.63^{+0.03}_{-0.03}$	$7.4 \times 10^{-6} - 7.4 \times 10^{-4}$
PS1-12brf	4	$0.65^{+0.23}_{-0.03}$	$+0.8^{+0.5}_{-1.5}$	$0.00^{+0.01}_{-0.01}$	$-17.94^{+0.08}_{-0.63}$	$9.2 \times 10^{-6} - 5.5 \times 10^{-4}$
PS1-10bjp	3	$0.40^{+0.03}_{-0.03}$	$+3.6^{+0.5}_{-0.5}$	$0.16^{+0.02}_{-0.02}$	$-17.20^{+0.03}_{-0.03}$	$2.7 \times 10^{-5} - 3.2 \times 10^{-4}$
$s = 0.6$						
PS1-10bjp <sup>b</sup>	11	$0.40^{+0.13}_{-0.03}$	$+5.2^{+0.5}_{-0.5}$	$0.16^{+0.03}_{-0.12}$	$-17.20^{+0.03}_{-0.03}$	$6.1 \times 10^{-3} - 4.2 \times 10^{-1}$
PS1-10ah	48	$0.35^{+0.18}_{-0.03}$	$+5.2^{+1.5}_{-7.5}$	$0.06^{+0.06}_{-0.07}$	$-16.63^{+0.03}_{-1.48}$	$4.3 \times 10^{-3} - 3.0 \times 10^{-2}$

<sup>a</sup>The number of templates fitting the multicolor light curves of candidates.<sup>b</sup>The best-fit template.

**Table 6.** Properties of candidates

Name	Likely origin	Location within galaxies	Probable transient templates	Photo- <i>z</i> consistent with DM	Consistent with detection in the beams	non-detection in other beams	ATCA source	VLA source	GMRT source	AGN nature WISE color	sig-in	Low-mass host galaxy	Star-forming host galaxy
Cand-1	AGN	Center	None	Yes	Yes		Yes	No	No	No		No	Yes
Cand-2	CCSN/RT	Off-center	RT SNe and IIn	Yes	Yes		No	No	No	Yes, but there are multiple galaxies		Yes	Yes
Cand-3	RT	Off-center	None, but reproduced with RTs with a faint peak and rapid decline	— <sup>a</sup>	Yes		No	No	No	— <sup>b</sup>		— <sup>a</sup>	— <sup>a</sup>
Cand-4	AGN	Center	None	Yes	Yes		No	No	No	No		No	Yes
Cand-5	AGN	Center	None	Yes	<b>No</b> <sup>c</sup>		No	No	No	No		No	No
Cand-6	CCSN/AGN	Center	SN IIn	<b>No</b> <sup>c</sup>	Yes		No	No	No	— <sup>b</sup>		No	Yes
Cand-7	AGN	Center	None	Yes	Yes		No	No	No	No		No	Yes
Cand-8	AGN	Center	None	Yes	Yes		No	No	No	No		No	Yes
Cand-9	AGN	Center	None	Yes	Yes		No	No	No	— <sup>b</sup>		No	Yes
Cand-10	AGN	Center	None	Yes	Yes		Yes	No	No	No		No	Yes
Cand-11	CCSN/AGN	Center	SN IIn	Yes	Yes		No	No	No	— <sup>b</sup>		No	Yes
Cand-12	AGN	Center	None	Yes	Yes		No	No	No	No		No	Yes
Cand-13	AGN	Center	None	Yes	Yes		No	No	No	No		No	Yes

<sup>a</sup>The fluxes of host galaxy cannot be derived due to the non-negligible contribution of the candidate to the total flux.

<sup>b</sup>No WISE source is found within the spatial resolution element of WISE.

<sup>c</sup>This excludes the candidate as an optical counterpart to FRB 151230.

**Table 7.** Templates fitting the light curves of transients outside the localization area of FRB 151230.

SN Type	Number <sup>b</sup>	Redshift	Name (separation <sup>a</sup> , photometric redshift)			$M_B$	$Q$ value
			$t_{\text{exp}}$	$E_B - V_{\text{host}}$ <sup>c</sup>	Stretch <sup>d</sup>		
Cand-14 (44.91 arcmin, photo- $z = 0.21^{+0.07}_{-0.16}$ )							
Nugent Ibc normal <sup>e</sup>	16	$0.20^{+0.08}_{-0.08}$	$-12.2^{+0.5}_{-2.3}$	$0.05^{+0.15}_{-0.05}$	$-16.05^{+0.03}_{-0.33}$	$1.0 \times 10^{-3} - 2.9 \times 10^{-3}$	
Cand-15 (41.17 arcmin, photo- $z = 0.55^{+0.06}_{-0.05}$ )							
Hsiao Ia <sup>e</sup>	280	$0.60^{+0.03}_{-0.13}$	$-14.5^{+19.0}_{-2.5}$	$1.20^{+0.01}_{-0.56}$	$0.65^{+0.13}_{-0.13}$	$-18.08^{+0.94}_{-0.55}$	$2.4 \times 10^{-3} - 6.3 \times 10^{-2}$
Nugent Ibc bright	102	$0.50^{+0.13}_{-0.03}$	$+4.0^{+2.5}_{-4.3}$	$0.26^{+0.07}_{-0.26}$	$-18.45^{+0.03}_{-0.03}$	$2.5 \times 10^{-3} - 5.2 \times 10^{-2}$	
Nugent Ibc normal	27	$0.60^{+0.03}_{-0.13}$	$+3.4^{+3.1}_{-1.5}$	$0.00^{+0.01}_{-0.00}$	$-18.05^{+0.63}_{-0.03}$	$2.6 \times 10^{-3} - 1.4 \times 10^{-2}$	
Nugent IIL normal	19	$0.55^{+0.08}_{-0.08}$	$-2.5^{+1.0}_{-1.0}$	$0.20^{+0.11}_{-0.20}$	$-17.91^{+0.80}_{-0.03}$	$2.4 \times 10^{-3} - 9.0 \times 10^{-3}$	
Cand-16 (28.41 arcmin, photo- $z = 0.47^{+0.14}_{-0.14}$ )							
Hsiao Ia <sup>e</sup>	18	$0.45^{+0.03}_{-0.03}$	$-14.7^{+8.1}_{-2.9}$	$1.15^{+0.06}_{-0.36}$	$0.75^{+0.03}_{-0.18}$	$-17.79^{+0.35}_{-0.73}$	$9.1 \times 10^{-3} - 1.3 \times 10^{-1}$
Nugent IIP	12	$0.55^{+0.08}_{-0.08}$	$-2.5^{+4.0}_{-1.0}$	$0.00^{+0.01}_{-0.00}$	$-18.01^{+0.33}_{-0.00}$	$9.2 \times 10^{-3} - 1.1 \times 10^{-1}$	
Nugent IIL normal	17	$0.60^{+0.03}_{-0.13}$	$-3.0^{+1.5}_{-0.5}$	$0.04^{+0.17}_{-0.04}$	$-17.91^{+0.50}_{-0.03}$	$9.0 \times 10^{-3} - 8.7 \times 10^{-2}$	
Nugent Ibc normal	1	$0.40^{+0.03}_{-0.03}$	$-7.4^{+0.5}_{-0.5}$	$0.00^{+0.01}_{-0.00}$	$-17.90^{+0.03}_{-0.03}$	$9.0 \times 10^{-3}$	
Cand-17 (46.15 arcmin, photo- $z = 0.33^{+0.22}_{-0.15}$ )							
Nugent Ibc bright <sup>e</sup>	75	$0.50^{+0.08}_{-0.08}$	$-30.0^{+7.3}_{-2.5}$	$0.01^{+0.14}_{-0.01}$	$-18.45^{+0.03}_{-0.38}$	$1.0 \times 10^{-2} - 9.7 \times 10^{-1}$	
Hsiao Ia	14162	$0.55^{+0.03}_{-0.38}$	$-49.3^{+35.9}_{-27.7}$	$1.20^{+0.01}_{-0.56}$	$0.30^{+0.48}_{-0.53}$	$-19.17^{+2.03}_{-1.12}$	$9.7 \times 10^{-3} - 8.7 \times 10^{-1}$
Nugent Ibc normal	160	$0.20^{+0.28}_{-0.03}$	$-33.2^{+10.5}_{-5.3}$	$0.00^{+0.01}_{-0.00}$	$-16.70^{+0.63}_{-1.38}$	$1.0 \times 10^{-2} - 8.6 \times 10^{-1}$	
Nugent IIL bright	186	$0.40^{+0.18}_{-0.03}$	$-25.0^{+18.0}_{-13.5}$	$0.00^{+0.01}_{-0.00}$	$-18.86^{+0.78}_{-0.63}$	$9.8 \times 10^{-3} - 1.4 \times 10^{-1}$	
Nugent IIP	45	$0.40^{+0.18}_{-0.03}$	$-27.0^{+20.0}_{-6.5}$	$0.00^{+0.01}_{-0.00}$	$-18.91^{+0.38}_{-0.03}$	$1.1 \times 10^{-2} - 1.2 \times 10^{-1}$	
Cand-18 (28.28 arcmin, -)							
Hsiao Ia <sup>e</sup>	65	$0.30^{+0.13}_{-0.08}$	$-51.2^{+20.1}_{-6.1}$	$1.10^{+0.11}_{-0.36}$	$-0.15^{+0.13}_{-0.08}$	$-19.78^{+0.70}_{-0.26}$	$3.4 \times 10^{-3} - 3.3 \times 10^{-1}$
Nugent IIL bright	1	$0.35^{+0.03}_{-0.03}$	$-8.5^{+0.5}_{-0.5}$	$0.00^{+0.01}_{-0.00}$	$-18.11^{+0.03}_{-0.03}$	$4.0 \times 10^{-3}$	
Cand-19 (29.12 arcmin, photo- $z = 0.88^{+0.11}_{-0.06}$ )							
Nugent IIn <sup>e</sup>	5	$0.90^{+0.08}_{-0.03}$	$+2.3^{+0.5}_{-1.2}$	$0.00^{+0.01}_{-0.00}$	$-18.21^{+0.08}_{-0.28}$	$6.7 \times 10^{-4} - 5.7 \times 10^{-3}$	
Cand-20 (22.71 arcmin, -)							
Hsiao Ia <sup>e</sup>	63	$0.60^{+0.03}_{-0.18}$	$+9.2^{+1.4}_{-1.1}$	$0.65^{+0.56}_{-0.01}$	$-0.20^{+0.23}_{-0.03}$	$-19.63^{+0.78}_{-0.71}$	$2.9 \times 10^{-3} - 2.9 \times 10^{-1}$
Cand-21 (32.90 arcmin, photo- $z = 0.28^{+0.32}_{-0.20}$ )							
Hsiao Ia <sup>e</sup>	22	$0.35^{+0.03}_{-0.18}$	$+10.8^{+0.5}_{-1.2}$	$0.75^{+0.46}_{-0.11}$	$-0.20^{+0.18}_{-0.03}$	$-19.46^{+0.42}_{-0.82}$	$2.0 \times 10^{-3} - 2.0 \times 10^{-1}$
Cand-22 (37.47 arcmin, photo- $z = 0.45^{+0.13}_{-0.26}$ )							
Hsiao Ia <sup>e</sup>	274	$0.55^{+0.03}_{-0.13}$	$+3.7^{+2.9}_{-10.4}$	$1.20^{+0.01}_{-0.51}$	$-0.15^{+0.18}_{-0.08}$	$-20.05^{+1.02}_{-0.29}$	$1.3 \times 10^{-5} - 1.3 \times 10^{-3}$
Cand-23 (46.41 arcmin, -)							
Nugent Ibc bright <sup>e</sup>	77	$0.65^{+0.08}_{-0.23}$	$-0.4^{+3.9}_{-3.3}$	$0.00^{+0.26}_{-0.00}$	$-18.80^{+0.38}_{-0.38}$	$6.7 \times 10^{-3} - 6.6 \times 10^{-1}$	
Hsiao Ia	123	$0.65^{+0.28}_{-0.18}$	$-3.1^{+4.8}_{-4.4}$	$0.80^{+0.41}_{-0.16}$	$0.30^{+0.43}_{-0.53}$	$-18.38^{+0.95}_{-1.96}$	$6.7 \times 10^{-3} - 2.0 \times 10^{-1}$
Nugent IIL normal	11	$0.40^{+0.13}_{-0.03}$	$-1.0^{+0.5}_{-1.5}$	$0.00^{+0.32}_{-0.00}$	$-16.89^{+0.08}_{-1.05}$	$7.0 \times 10^{-3} - 5.6 \times 10^{-2}$	
Cand-24 (38.75 arcmin, photo- $z = 0.56^{+0.06}_{-0.33}$ )							
Nugent Ibc normal <sup>e</sup>	158	$0.35^{+0.23}_{-0.13}$	$+4.4^{+3.1}_{-8.3}$	$0.00^{+0.15}_{-0.00}$	$-16.65^{+0.63}_{-1.33}$	$9.4 \times 10^{-3} - 8.6 \times 10^{-1}$	
Hsiao Ia	862	$0.60^{+0.03}_{-0.18}$	$-0.5^{+9.1}_{-1.5}$	$1.20^{+0.01}_{-0.56}$	$0.20^{+0.43}_{-0.23}$	$-19.00^{+1.29}_{-0.61}$	$8.6 \times 10^{-3} - 5.6 \times 10^{-1}$
Nugent IIP	24	$0.25^{+0.28}_{-0.03}$	$+1.5^{+4.0}_{-1.5}$	$0.00^{+0.01}_{-0.00}$	$-15.41^{+0.13}_{-1.93}$	$8.8 \times 10^{-3} - 2.8 \times 10^{-1}$	
Nugent IIL normal	97	$0.30^{+0.23}_{-0.08}$	$+0.0^{+5.5}_{-1.0}$	$0.21^{+0.24}_{-0.21}$	$-16.44^{+0.03}_{-1.58}$	$9.0 \times 10^{-3} - 1.6 \times 10^{-1}$	
Nugent Ibc bright	2	$0.50^{+0.03}_{-0.03}$	$+0.0^{+0.5}_{-0.5}$	$0.22^{+0.02}_{-0.22}$	$-18.45^{+0.03}_{-0.03}$	$1.0 \times 10^{-2} - 1.2 \times 10^{-2}$	
Cand-25 (34.11 arcmin, photo- $z = 0.33^{+0.18}_{-0.19}$ )							
Nugent IIP <sup>e</sup>	16	$0.45^{+0.08}_{-0.03}$	$-0.5^{+1.5}_{-1.0}$	$0.00^{+0.01}_{-0.00}$	$-17.36^{+0.08}_{-0.53}$	$1.5 \times 10^{-5} - 6.4 \times 10^{-4}$	
Cand-26 (33.91 arcmin, photo- $z = 0.31^{+0.03}_{-0.02}$ )							
Nugent Ibc normal <sup>e</sup>	3	$0.30^{+0.03}_{-0.03}$	$-4.8^{+0.5}_{-0.5}$	$0.00^{+0.01}_{-0.00}$	$-16.60^{+0.08}_{-0.08}$	$1.4 \times 10^{-6} - 2.9 \times 10^{-6}$	
Cand-27 (48.41 arcmin, photo- $z = 0.64^{+0.08}_{-0.07}$ )							
Nugent Ibc bright <sup>e</sup>	73	$0.65^{+0.08}_{-0.08}$	$-42.4^{+6.7}_{-78.7}$	$0.00^{+0.01}_{-0.00}$	$-20.15^{+0.43}_{-0.18}$	$3.7 \times 10^{-4} - 2.0 \times 10^{-2}$	
Cand-28 (25.48 arcmin, photo- $z = 0.41^{+0.09}_{-0.07}$ )							
Hsiao Ia <sup>e</sup>	72	$0.35^{+0.03}_{-0.03}$	$+10.8^{+0.5}_{-1.5}$	$1.10^{+0.11}_{-0.31}$	$0.00^{+0.08}_{-0.13}$	$-19.68^{+0.75}_{-0.10}$	$8.3 \times 10^{-3} - 8.1 \times 10^{-1}$
PS1-10bjp	4	$0.35^{+0.08}_{-0.03}$	$+9.9^{+0.5}_{-0.6}$	$0.26^{+0.02}_{-0.26}$	$-17.20^{+0.03}_{-0.03}$	$1.8 \times 10^{-2} - 4.6 \times 10^{-1}$	
PS1-10ah	3	$0.35^{+0.03}_{-0.03}$	$+9.9^{+0.5}_{-0.5}$	$0.14^{+0.02}_{-0.14}$	$-16.63^{+0.03}_{-0.03}$	$1.9 \times 10^{-2} - 1.5 \times 10^{-1}$	
Cand-29 (27.95 arcmin, photo- $z = 0.73^{+0.17}_{-0.12}$ )							
Nugent Ibc bright <sup>e</sup>	20	$0.65^{+0.08}_{-0.03}$	$-6.4^{+4.5}_{-2.3}$	$0.00^{+0.01}_{-0.00}$	$-18.90^{+0.33}_{-0.58}$	$5.4 \times 10^{-3} - 4.2 \times 10^{-1}$	
Hsiao Ia	307	$0.90^{+0.03}_{-0.28}$	$-13.3^{+10.3}_{-7.5}$	$0.95^{+0.26}_{-0.31}$	$-0.15^{+0.63}_{-0.08}$	$-19.74^{+1.30}_{-0.39}$	$5.2 \times 10^{-3} - 9.4 \times 10^{-2}$
Cand-30 (30.75 arcmin, photo- $z = 0.67^{+0.06}_{-0.05}$ )							
PS1-10ah <sup>e</sup>	4	$0.65^{+0.08}_{-0.03}$	$+7.1^{+0.5}_{-0.7}$	$0.00^{+0.01}_{-0.00}$	$-17.78^{+0.03}_{-0.23}$	$2.0 \times 10^{-5} - 5.6 \times 10^{-5}$	
Cand-31 (18.65 arcmin, photo- $z = 0.34^{+0.02}_{-0.03}$ )							
Nugent Ibc bright <sup>e</sup>	15	$0.35^{+0.03}_{-0.03}$	$-81.6^{+3.5}_{-2.5}$	$0.00^{+0.01}_{-0.00}$	$-20.30^{+0.18}_{-0.03}$	$1.3 \times 10^{-3} - 1.7 \times 10^{-2}$	
Nugent IIn	241	$0.35^{+0.03}_{-0.03}$	$-70.5^{+5.5}_{-45.5}$	$0.00^{+0.01}_{-0.00}$	$-18.86^{+0.43}_{-1.83}$	$1.2 \times 10^{-3} - 1.6 \times 10^{-2}$	
Cand-32 (21.76 arcmin, photo- $z = 0.54^{+0.10}_{-0.06}$ )							

Table 7. (Continued)

SN Type	Number <sup>b</sup>	Redshift	Name (separation <sup>a</sup> , photometric redshift)		$E_{B-V, \text{host}}^c$	$M_B$	$Q$ value
			$t_{\text{exp}}$				
Nugent Ibc normal <sup>e</sup>	58	$0.50^{+0.13}_{-0.03}$	$+8.0^{+0.7}_{-3.1}$		$0.00^{+0.01}_{-0.00}$	$-17.55^{+0.58}_{-0.53}$	$4.5 \times 10^{-3} - 1.6 \times 10^{-1}$
Nugent Ibc bright	151	$0.50^{+0.13}_{-0.03}$	$+8.0^{+1.5}_{-4.3}$		$0.28^{+0.28}_{-0.28}$	$-18.45^{+0.03}_{-0.03}$	$4.0 \times 10^{-3} - 1.6 \times 10^{-1}$
Nugent IIL normal	57	$0.55^{+0.08}_{-0.08}$	$-1.5^{+2.5}_{-1.0}$		$0.54^{+0.14}_{-0.54}$	$-17.91^{+0.03}_{-0.03}$	$4.1 \times 10^{-3} - 1.8 \times 10^{-2}$
PS1-12brf	47	$0.50^{+0.08}_{-0.03}$	$+1.8^{+2.5}_{-0.6}$		$0.30^{+0.05}_{-0.30}$	$-17.39^{+0.03}_{-0.03}$	$4.0 \times 10^{-3} - 9.0 \times 10^{-3}$

<sup>a</sup>Separation from the center of the localization area of FRB 151230.

<sup>b</sup>The number of templates fitting the multicolor light curves of candidates.

<sup>c</sup>Color excess of the host galaxy for the CCSN and RT templates.

<sup>d</sup>Stretch and color parameters for the SN Ia templates.

<sup>e</sup>The best-fit template.

**Table 8.** Parameters of templates.

Parameter	Range	Step
Type Ia SN		
Color $c$	$-0.2 - +0.8$	0.05
Stretch $s$	$0.6 - 1.2$	0.01
Intrinsic variation $I$	$-0.3 - +0.3$	0.05
Redshift $z$	$0 - 2$	0.05
Type IIP SN		
Peak magnitude $M_B$	$-14.43 - -18.91$	0.05
Color excess $E_{B-V,host}$	$0.0 - 1.0$	0.01
Redshift $z$	$0 - 2$	0.05
Type IIL normal SN		
Peak magnitude $M_B$	$-16.47 - -17.99$	0.05
Color excess $E_{B-V,host}$	$0.0 - 1.0$	0.01
Redshift $z$	$0 - 2$	0.05
Type IIL bright SN		
Peak magnitude $M_B$	$-17.92 - -19.96$	0.05
Color excess $E_{B-V,host}$	$0.0 - 1.0$	0.01
Redshift $z$	$0 - 2$	0.05
Type IIn SN		
Peak magnitude $M_B$	$-16.98 - -20.66$	0.05
Color excess $E_{B-V,host}$	$0.0 - 1.0$	0.01
Redshift $z$	$0 - 4$	0.05
Type Ibc normal SN		
Peak magnitude $M_B$	$-16.09 - -17.95$	0.05
Color excess $E_{B-V,host}$	$0.0 - 1.0$	0.01
Redshift $z$	$0 - 2$	0.05
Type Ibc bright SN		
Peak magnitude $M_B$	$-18.46 - -20.30$	0.05
Color excess $E_{B-V,host}$	$0.0 - 1.0$	0.01
Redshift $z$	$0 - 2$	0.05
Rapid transient (PS1-10ah)		
Peak magnitude $M_B$	$-16.63 - -18.63$	0.05
Color excess $E_{B-V,host}$	$0.0 - 1.0$	0.01
Redshift $z$	$0 - 2$	0.05
Rapid transient (PS1-10bjp)		
Peak magnitude $M_B$	$-17.20 - -19.20$	0.05
Color excess $E_{B-V,host}$	$0.0 - 1.0$	0.01
Redshift $z$	$0 - 2$	0.05
Rapid transient (PS1-11qr)		
Peak magnitude $M_B$	$-18.03 - -20.03$	0.05
Color excess $E_{B-V,host}$	$0.0 - 1.0$	0.01
Redshift $z$	$0 - 2$	0.05
Rapid transient (PS1-12bv)		
Peak magnitude $M_B$	$-18.44 - -20.44$	0.05
Color excess $E_{B-V,host}$	$0.0 - 1.0$	0.01
Redshift $z$	$0 - 2$	0.05
Rapid transient (PS1-12brf)		

**Table 8.** (Continued)

Parameter	Range	Step
Peak magnitude $M_B$	$-17.39 - -19.39$	0.05
Color excess $E_{B-V, \text{host}}$	$0.0 - 1.0$	0.01
Redshift $z$	$0 - 2$	0.05